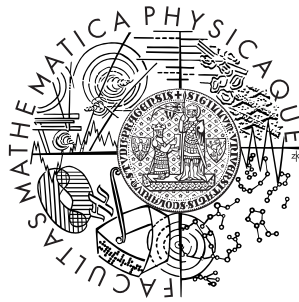


Charles University in Prague
Faculty of Mathematics and Physics

DIPLOMA THESIS



Jitka Vrátná

Physical Properties of Ultrafine-grained Polycrystals of Magnesium Based Alloys

Department of Physics of Materials

Supervisor: Assoc. Prof. Miloš Janeček

Study Program: Physics of Condensed Systems and Physics of Materials

2010

Acknowledgement

I would like to express my appreciation above all to my supervisor Assoc. Prof. Miloš Janeček. My sincere thanks are also extended to Dr. Král, Prof. Lukáč, Assoc. Prof. Čížek and Assoc. Prof. Hadzima for their consultations. My gratitude also goes to J. Stráský, M. Čepová, V. Škorík and M. Bukovina, who supported me in my scientific work. Finally, I would like to thank the Grant Agency of the Charles University for financial support in the form of the research project number 59409.

Prohlášení

Prohlašuji, že jsem svou diplomovou práci vypracovala samostatně a použila pouze podklady uvedené v příloženém seznamu.

Nemám závažný důvod proti užití tohoto školního díla ve smyslu §60 Zákona č. 121/2000 Sb., o právu autorském, o právech souvisejících s právem autorským a o změně některých zákonů (autorský zákon).

V Praze dne

Title: Physical Properties of Ultrafine-grained Polycrystals of Magnesium Based Alloys
Author: Jitka Vrátná
Department: Department of Physics of Materials
Supervisor: Assoc. Prof. Miloš Janeček
Supervisor's e-mail address: Milos.Janecek@mff.cuni.cz

Abstract: The objective of the thesis is the study of microstructure evolution, mechanical properties, defect structure and corrosion resistance of ultra-fine grained magnesium alloy AZ31 prepared by a combined two-step process: the extrusion and the equal-channel angular pressing (ECAP). The microstructure development was studied using light and transmission electron microscopy and electron backscatter diffraction (EBSD). Mechanical properties were studied by microhardness measurement and tensile tests and the defect structure by positron annihilation spectroscopy (PAS). The results of tensile tests indicates that the characteristic stress $\sigma_{0.2}$ increases slightly with increasing number of ECAP passes only to the second pass and then decreases significantly with additional ECAP straining. This behaviour is in accordance with the results of PAS. EBSD measurements show that the microstructure of extruded and ECAPed material has a bimodal distribution of grain sizes. The bimodal distribution becomes homogeneous with increasing number of ECAP passes and no remaining large grains are observed after 8 passes. The average grain size in the specimen after 8 passes is in the submicrometer range and the fraction of high-angle grain boundary (HAGB) is approximately 80%. The extruded specimens after 8 ECAP passes show the best corrosion resistance from all investigated samples mainly due to its homogenous microstructure and a low density of microcracks in ECAPed specimens.

Keywords: ultra-fine grained Mg-based alloys, SPD processes, ECAP, microstructure evolution, corrosion resistance

Název práce: Fyzikální vlastnosti ultrajemnozrných polykrystalů slitin na bázi hořčíku
Autor: Jitka Vrátná
Katedra (ústav): Katedra fyziky materiálů
Vedoucí diplomové práce: Doc. RNDr. Miloš Janeček, CSc.
E-mail vedoucího: Milos.Janecek@mff.cuni.cz

Abstrakt: Předložená diplomová práce se zabývá studiem mikrostruktury, mechanickými vlastnostmi, strukturou poruch a korozní odolností ultrajemnozrné hořčíkové slitiny AZ31 připravené dvěma po sobě jdoucími procesy: extruzí a metodou ECAP. Vývoj mikrostruktury byl studován pomocí optické a transmisní elektronové mikroskopie a pomocí difrakce zpětně odražených elektronů (EBSD). Mechanické vlastnosti byly zkoumány měřením mikrotvrdosti a tahovými zkouškami, struktura poruch byla pozorována metodou pozitronové anihilační spektroskopie (PAS). Z tahových zkoušek bylo zjištěno, že charakteristické napětí $\sigma_{0.2}$ slabě roste pouze do dvou průchodů ECAP a s každým dalším průchodem poměrně výrazně klesá. Tento průběh napětí $\sigma_{0.2}$ odpovídá naměřeným výsledkům z PAS. Měření EBSD prokázalo, že materiál obsahuje bimodální strukturu - skládá se z menšího množství velkých zrn, které jsou obklopené malými zrny. Tato bimodální struktura s rostoucím počtem průchodů postupně mizí. Po 8 průchodech již nejsou pozorována žádná hrubá zrna, struktura je homogenní a průměrná velikost zrn se pohybuje v submikronové oblasti. Podíl vysokoúhlových hranic zrn je přibližně 80%. Nejlepší korozní odolnosti ze všech studovaných vzorků bylo dosaženo u vzorku po osmi průchodech ECAP. Tato relativně vysoká odolnost proti korozi je způsobena hlavně homogenní mikrostrukturou a relativně malým výskytem mikrotrhlin ve vzorku po osmi průchodech.

Klíčová slova: jemnozrné hořčíkové slitiny, SPD procesy, metoda ECAP, vývoj mikrostruktury, korozní odolnost

Table of contents

1	Introduction	6
1.1	Magnesium and its alloys	7
1.2	SPD processes	10
1.2.1	ECAP	11
1.2.2	High Pressure Torsion	17
1.2.3	Accumulative Roll-Bonding	18
1.3	Important properties of UFG materials processed by SPD	19
2	Aims of the thesis	21
3	Experimental Procedures	22
3.1	Experimental material	22
3.2	Light microscopy	23
3.3	Microhardness measurements	23
3.4	Tensile tests	24
3.5	Positron annihilation spectroscopy	25
3.6	EBSD	25
3.7	Transmission electron microscopy	26
3.8	Corrosion tests	28
4	Experimental results and discussion	30
4.1	Microstructure after ECAP	30
4.2	Mechanical properties	31
4.2.1	Microhardness	31
4.2.2	Tensile properties	31
4.3	Microstructure and defect structure evolution using PAS	36
4.4	Microstructural characterization using EBSD	39
4.5	Microstructural characterization using TEM	43
4.6	Corrosion properties	46
5	Conclusions	52
6	Prospective continuation of the research	53
7	Bibliography	54

1 Introduction

Magnesium is one of the lightest metals used in constructional alloys. Replacing aluminum and steel with magnesium in the same volumes would result in a weight saving of around 33% and 77%, respectively. The significant weight saving ability offers potential for industrial production of automotive or aircraft components. The use of magnesium alloys in manufacturing automobile components started as early as before the Second World War. Nevertheless the production and applications of magnesium have not grown much because of the limited use of wrought magnesium alloys. On the other hand, magnesium alloys have good casting properties and that is why cast magnesium alloys have successfully replaced aluminum alloys and steels in many applications (e.g. engine blocks and other automobile components). Wrought magnesium alloys have not been able to replace aluminum because of their hexagonal closed packed lattice and therefore limited active slip systems. However, significant advances have been made in the field of wrought magnesium alloys in last few years. At elevated temperature, the additional slip systems is activated and the formability of magnesium is improved. The wrought magnesium alloys have finer grain sizes after recrystallization and have therefore higher strength and ductility in comparison with as-cast alloys.

Cast magnesium alloys suffer from inhomogeneous coarse grain sizes. When the alloy is prepared by high pressure die casting, the grain sizes are usually fine because of significantly high cooling rates. When the cooling rate is relatively low (e.g. during the sand casting), the grain refining agent is required to get a uniform fine microstructure [1]. Aluminum alloying is one of the most widely used methods of grain refinement in magnesium alloys. Aluminum contributes in strength by solid solution strengthening and precipitate hardening. The strength of Mg-Al alloys can be further increased by addition of third alloying element. However, this technique cannot be used when the alloy contains elements which form stable compounds with aluminum. Another method of grain refinement in magnesium alloys is the zirconium addition.

Magnesium has closed packed hexagonal crystal lattice with parameters $a = 0.320 \text{ nm}$, $c = 0.520 \text{ nm}$ and an axial ratio $\frac{c}{a} = 1.624$. At room temperature, the (0001) basal slip is the most active slip system. Because of fewer number of slip systems in hexagonal closed packed lattice, basal slip does not offer five independent slip systems which are required for uniform deformation according to von-Mises criterion [2]. The deformation twinning provides the additional independent deformation mode at room temperature. At elevated temperatures, the critical shear stresses for prismatic and pyramidal slip systems reduce significantly and the twinning contribution becomes less crucial. Therefore, magnesium alloys have to be deformed at elevated temperatures to activate other slip systems in addition to the basal slip. Various conventional deformation methods are employed for the deformation of magnesium alloys, e.g. extrusion, rolling, forging, and severe plastic deformation methods (see chapter 1.2). Some conventional methods are already in use at the industrial levels and can be readily applied to magnesium alloys, some methods are still used at the laboratory scale only.

Mg alloys can undergo dynamic recrystallization upon the deformation process (e.g. extrusion or rolling). It is believed that even at low deformation temperatures, the rise in internal energy is enough to cause the dynamic recrystallization. The recrystallization and thus the microstructure evolution is affected by the deformation parameters.

Temperature is one of the most important conditions. At lower temperatures, twinning is more active, new grains nucleate at the twin interfaces and a fine grain size is achieved. At higher temperatures, new grains nucleate at the original grain boundaries and a relatively coarse grain size is achieved [3].

The homogenization heat treatment is in general performed to remove the segregation of alloying elements that occurs due to non-equilibrium cooling during the casting process. In magnesium alloys with aluminum and zinc (AZ class) the homogenization treatment removes the micro-segregation of Al and Zn elements [4]. It leads to increases in hardness, UTS and elongation, without any loss of corrosion resistance [5]. In dependence on the treatment temperature, the homogenization treatment dissolves the eutectic and other intermetallic phases and affects the deformation and recrystallization behaviour. Nucleation and growth parts of the recrystallization are affected by the second phase particles; it depends on their sizes and interparticle distances. Lower interparticle distance is more effective in pinning the boundaries during the grain growth. An effective control of the second phase particles can almost randomize the texture in wrought magnesium alloys [6].

1.1 Magnesium and its alloys

The first commercial production of magnesium commenced in the middle of the 19th century. Consequently, the first magnesium alloys were developed. Magnesium alloys were significantly used during the Second World War. However, there was no steady development as in the case of aluminum alloys. The number of aluminum alloys is much higher than the number of magnesium alloys. Due to the environmental policy and the rising fuel costs, the low density of magnesium alloys is attractive enough to shift the focus again on magnesium alloys as a constructional material. Some of the magnesium alloys are also biocompatible and applicable in medicine, e.g. temporary screw, wire fixation or biodegradable stents.

The usual alloying elements in magnesium alloys are aluminum, zinc, manganese, zirconium and rare earth metals. They mainly improve the strength both at room temperature and at elevated temperatures. Magnesium cast alloys may contain up to 10% aluminum, up to 6.5% zinc, up to 0.5% manganese, up to 1.5% silicon and traces of copper, nickel and iron. Special alloys have additions of rare earth elements up to 4%. Silver and zirconium may be also added (up to 3% and 1%, respectively). Newly developed alloys can have contents of rare earth elements up to 10% and high levels of lithium.

Wrought alloys have up to 10% aluminum, up to 2% manganese, up to 6% zinc, upto 1.5% silicon and traces of copper, nickel and iron. Though present in traces, the concentration of the heavy metals (copper, nickel and iron) is very important for corrosion properties. The concentration of these metals should be less than 0.05% to achieve high corrosion resistance.

Magnesium alloys can be classified based on their dominant properties. The addition of light metal (e.g. aluminum) in magnesium keeps the specific weight low and makes the super light alloy. Good creep properties in magnesium alloys are achieved by introducing zirconium, scandium or rare earth metals. These alloying elements form intermetallic compounds among themselves and thereby stabilize the microstructure

at elevated temperatures.

Magnesium has very good casting properties, but poor workability, especially at room temperature. Therefore, more casting alloys are available than wrought alloys in the market. However, wrought magnesium alloys have high strength which can be further enhanced by special thermomechanical treatments. Wrought magnesium alloys exhibit much better combination of strength and ductility than the cast alloys [7], but most of the magnesium alloys are used in as-cast form.

Magnesium and its alloys have good fluidity and melting point at 923 K. On the other hand, magnesium alloys have poor capability to deform due to their hexagonal closed packed lattice. This crystal structure provides only fewer independent slip systems, which makes deformation difficult. Additional slip systems are activated at elevated temperature and the formability of wrought magnesium alloys improves. Typically deformation temperature used for magnesium alloys varies between 300 and 400 °C. The upper level for deformation temperature is affected by the presence of intermetallic phases having low reaction temperatures. For example, in AZ magnesium alloys, the eutectic phase $Mg_{17}Al_{12}$ has a melting point of approximately 435 °C. Therefore, in order to avoid the incipient melting of the eutectic phase during deformation, temperatures cannot exceed this level.

Two deformation mechanisms are observed in magnesium structure: slip and twinning. Deformation by slip occurs on distinctive lattice planes called slip planes in certain slip direction which are characteristic for a certain crystal structure. The slip directions are usually the crystallographic directions with the shortest distance between atoms or ions and the slip planes are usually densely packed planes. The magnitude of the shear displacement is an integral multiple of interatomic distances, so that the lattice remains unchanged after slip. On the other hand, deformation twinning introduces distortions in the original lattice, but the contribution of deformation twinning in total strain is much lower than that of crystallographic slip. However, this little contribution is significant in the sense that these changes in the lattice caused by twinning may orient the lattice to favor further slip.

The crystallographic slip is initiated when the stress applied on slip plane is higher than the critical resolved shear stress. Slip systems in magnesium lattice can be categorized on the basis of slip direction as either slip or slip systems. The basal and prismatic slip planes belong to the type slip systems. In contrast, the pyramidal slip planes can be either $\langle a \rangle$ or $\langle c + a \rangle$ types.

In a polycrystalline material, each grain must deform with the same external strains as the whole polycrystal. For an individual grain this amounts to an imposed set of strains along the crystal axes. Five independent strains describe an arbitrary strain state or shape change. According to the Von Mises criterion, five independent slip systems must be active in polycrystals to avoid overlaps and void formations. A slip system is independent, if the shape change made by that system cannot be achieved by a combination of other slip systems. If a material has less than five independent slip systems, another deformation mechanism will be activated to achieve homogeneous deformation of polycrystal. Independent slip systems of magnesium are shown in Tab. 1.1.

Direction	Plane	Slip system	Independent modes
$\langle a \rangle$	Basal plane	(0002) $\langle 11\bar{2}0 \rangle$	2
$\langle a \rangle$	Prismatic plane	(1 $\bar{1}$ 00) $\langle 11\bar{2}0 \rangle$	2
$\langle a \rangle$	Pyramidal plane	(1 $\bar{1}$ 0 l) $\langle 11\bar{2}0 \rangle$	4
$\langle c + a \rangle$	Pyramidal plane	(1 $\bar{1}$ 0 l) $\langle 11\bar{2}3 \rangle$	5

Table 1.1: Independent slip systems in magnesium

The closed packed hexagonal lattice of magnesium has an axial ratio of 1.624. This implies that $\langle 11\bar{2}0 \rangle$ crystallographic direction, which lies in the basal plane, is the shortest in the magnesium lattice. Therefore, most of the dislocations glide in this direction. The basal slip system is the most active slip system in magnesium because the reported critical resolved shear stress for basal slip is only 0.5 MPa [8]. However, due to the low symmetry of hexagonal closed packed lattice, basal slip system provides only two independent slip systems and the von Mises criterion is not met. The activity of a non-basal slip system must be increased to achieve appreciable formability of magnesium alloys. The magnitude of critical resolved shear stress for non-basal slip depends on solute atoms, precipitates and deformation temperature [9].

At elevated temperatures, other slip systems in addition to the basal type are activated. The magnitude of critical resolved shear stress of the prismatic slip in magnesium decreases with increasing temperature. At room temperature it is about 100 times higher than that of the basal slip, whereas at 300 °C, it is only four times higher [10]. Activation of (1 $\bar{1}$ 00) $\langle 11\bar{2}0 \rangle$ prismatic slip system provides two additional independent slip systems. After that, the number of independent slip systems is four, which does not meet the von Mises criterion either. The $\langle c + a \rangle$ slip (the second order pyramidal slip) has four independent slip systems and except deformation twinning, it is the only slip system which imparts deformation along the c -axis of the lattice.

Deformation twinning is a very important deformation mechanism. A deformation twin is a region of a crystal which had undergone a homogeneous shape deformation in such a way that the resulting product structure is identical to that of the parent but oriented differently. In comparison with slip, deformation by twinning produces a homogeneous shear uniformly distributed over a three-dimensional region. The shear deformation caused by twinning is small and limited but it can be significant in its effects. At the beginning of plastic deformation, twins act as obstacles for basal slip in hexagonal closed packed metal and thus cause strain hardening [11]. At later stages of plastic deformation, twinning may reorient the basal planes and thereby make them favorable for slip.

The contribution of deformation twinning is important at low temperatures because of the only active slip system is the basal slip. Additional slip systems are activated with increasing temperature and the contribution of twinning in the deformation process becomes less critical. Twinning is also important during recrystallization because twin interfaces provide additional nucleation sites and thereby give fine grain size by increasing the rate of nucleation.

1.2 SPD processes

The ultra-fine grained (UFG) materials are characterized by very small grain sizes (in the submicrometer and the nanometer range), homogeneous and equiaxed microstructure and a high fraction of high angle grain boundaries [12]. Nowadays the most common procedures for the fabrication UFG materials are severe plastic deformation (SPD) processes. The reduction of grain size in polycrystalline materials results in changes in mechanical and other physical properties. The strength of a polycrystalline material is related to the grain size d according to the Hall-Petch equation [13, 14]

$$\sigma_y = \sigma_0 + k_y d^{-1/2}, \quad (1.1)$$

where σ_y represents the yield stress of the material, σ_0 is termed the friction stress and k_y is a material constant. The fact that the strength increases with a reduction of grain size is the reason of the present interest in production of UFG materials.

Currently two basic approaches for the fabrication of bulk UFG materials are known. These are reported as the "bottom-up" and the "top-down" approach [15].

The base of the "bottom-up" approach is to produce ultra-fine powders and to consolidate them. The methods applying this approach are, for example, the electrodeposition [16], inert gas condensation [17], ball milling [18] or cryomilling [19]. Material with extremely small grain size may be obtained by these techniques. However, the disadvantage of these techniques is some degree of residual porosity in the material and potential contamination.

The "top-down" approach is an inverse process to the "bottom-up" approach. In this case, a bulk solid with a relatively coarse grain size is processed to introduce very high strains into the material and to produce UFG material. Almost no porosity and contamination were observed in these materials. Rolling, forging and extrusion are known to be some of the conventional methods of grain size reduction. UFG materials are hardly achieved by these methods. The main problem is to introduce high deformation energy in the specimen and do not change its geometry, in particular to reduce its cross-section. New modern methods have been developed recently to overcome this problem. These methods are generally described as severe plastic deformation (SPD).

One of the first SPD procedures appeared in ancient China. The legendary Bai-Lian steel swords were produced by this technique [20]. Subsequently, this skill was spread to India for the production of the ultra-high carbon Wootz steel [21] and thereafter to Syria for production of the world-famous Damascus steel [22]. The first scientific approach to SPD processes was introduced by Bridgman in the 1940s and 1950s [23]. Since that time, a lot of more or less useful SPD procedures were developed and investigated. The most frequently used current techniques of SPD are equal-channel angular pressing (ECAP) [24], high-pressure torsion (HPT) [25, 26], accumulative roll-bonding (ARB) [27], friction stir processing (FSP) [28, 29], repetitive corrugation and straightening (RCS) [30, 31], multi-directional forging [32, 33], twist extrusion [34, 35] or reciprocating extrusion [36, 37], etc. These techniques will be described in the following section.

1.2.1 ECAP

The equal-channel angular pressing (ECAP), known also as equal-channel angular extrusion (ECAE), is currently the most developed SPD procedure. ECAP was invented by Segal et al. in 1970s and 1980s in the former Soviet Union [38, 24]. Since its invention this technique became well-known and world-widely used by many scientists. ECAP was successfully applied to produce ultra-fine grain material structure in a large variety of pure metals and their alloys, for example UFG magnesium [39], aluminum [40], copper [41], nickel [42], titanium [43], steels [44], and more complicated materials, e.g. duplex steels and metal-matrix composites [45]. At present, ECAP is a promising SPD technique applicable in many branches of industry.

The advantage of ECAP in comparison with other SPD techniques is mainly the same cross-sectional dimensions of the specimen after the pressing. This design allows repetitive pressing and the accumulation of strain in the specimen. Furthermore, the ECAP is a quite simple process. However, the ECAP technique has some limitations. Unlike direct extrusion where almost any length of the rod may be processed in ECAP limited specimen length may be pressed through the die. Generally the billets length varies between 5 and 15 cm. In addition, the ends of processed billets usually contain heterogeneous microstructure and crack formation may occur. Therefore these parts of the billets have to be removed after each pass. Last but not least the ECAPed material is quite expensive. The invention of conform ECAP solved this problem [46]. The principle of conform ECAP will be described below.

The ECAP die consists of two channels with the same cross-section. Generally, the ECAP die is characterized by two angles: Φ , which is formed by these two channels and the angle Ψ , which indicates the outer arc of curvature at the intersection of the two channels. The conventional mostly used ECAP die with the angle Φ equal to 90° is shown schematically in Fig. 1.1 and the general ECAP die with the illustration of the both angles is shown in Fig. 1.2.

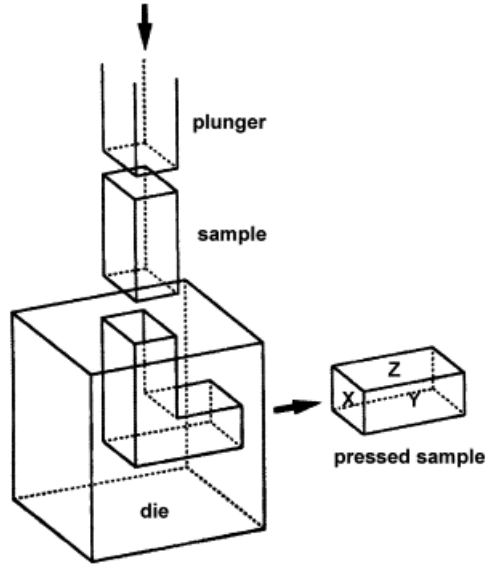


Figure 1.1: Schematic illustration of a conventional ECAP facility, X denotes the transverse plane, Y flow plane and Z the longitudinal plane [47]

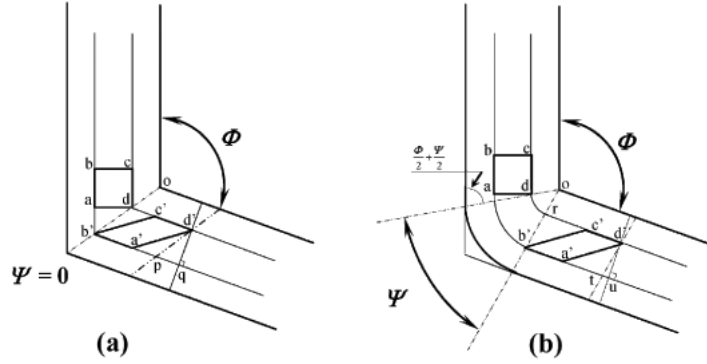


Figure 1.2: The scheme of pressing of the rectangular sample with the square cross-section through the ECAP die a) with $\Psi = 0$ and b) $\Psi \neq 0$ [48].

The sample pressed through the die is deformed by a simple shear in the intersection point of the channels and the imposed strain after N passes is expressed [48]

$$\epsilon_N = \frac{N}{\sqrt{3}} \left[2\cot\left(\frac{\Phi}{2} + \frac{\Psi}{2}\right) + \Psi\operatorname{cosec}\left(\frac{\Phi}{2} + \frac{\Psi}{2}\right) \right]. \quad (1.2)$$

The equivalent strain imposed on the specimen during one pass in ECAP depends on both angles. However the angle Φ has the dominant effect. The equivalent strain ϵ after one pass in the conventional ECAP with $\Psi = 90^\circ$ is close to ~ 1 cf. Fig. 1.3.

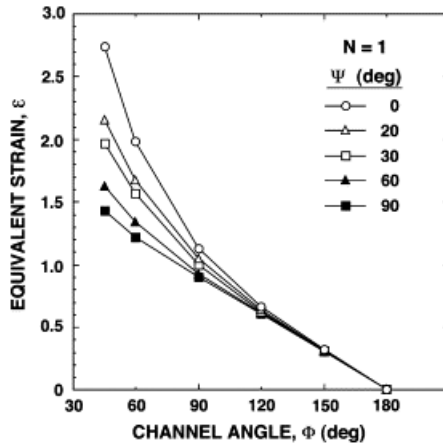


Figure 1.3: The equivalent strain ϵ after one pass of ECAP as a function of the angles Φ and Ψ [49].

As mentioned above, the same cross-section of both channels allows repetitive pressing of the specimen. The multiple pressing results in the accumulation of the equivalent strain which is necessary to produce an UFG material. On the other hand, the higher number of ECAP passes could cause cracking or other material defects formation especially when not optimal temperature and pressing speed is employed. As a consequence, the optimal number of passes depends on the material structure and the processing parameters.

In most cases, the billets with square cross-sections and the dies with square channels are used. The square cross-section of channels allows various sample rotations between the individual passes which are known as routes [50]. Pressing through different routes activates different slip systems in the consecutive passes [51] and leads to different microstructures. Four different processing routes, schematically shown in Fig. 1.4 may be used [52]. In route A the specimen is pressed without rotation between the passes, in route B_A the specimen is rotated by 90° in alternate directions, while in route B_C the specimen is rotated by 90° in the same direction and in route C the specimen is rotated by 180° between the consecutive passes.

The slip systems activated during ECAP are illustrated in Fig. 1.5. X, Y and Z planes are the orthogonal planes shown in Fig. 1.1 and the numbers 1-4 correspond to the number of passes [53]. The activation of slip systems depends on the route employed. In routes C and B_C , the shearing planes are the same in each pass while the shear direction is opposite. Thus, the equivalent strain is compensated after every even number of passes. On the other hand, the slip systems in routes A and B_A are different and the strain is accumulated during consecutive passes. However, it is not apparent which route is optimal for producing UFG materials. Nowadays, the major part of experimental investigation was done in materials processed by B_C route, because it was found to produce the finest and relatively equiaxed grains with a high fraction of high-angle grain boundaries.

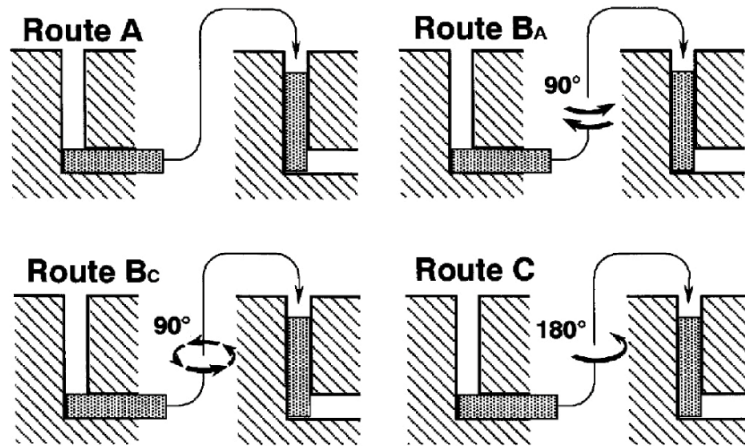


Figure 1.4: The four basic pressing routes in the ECAP die with square cross-sectional channels [52].

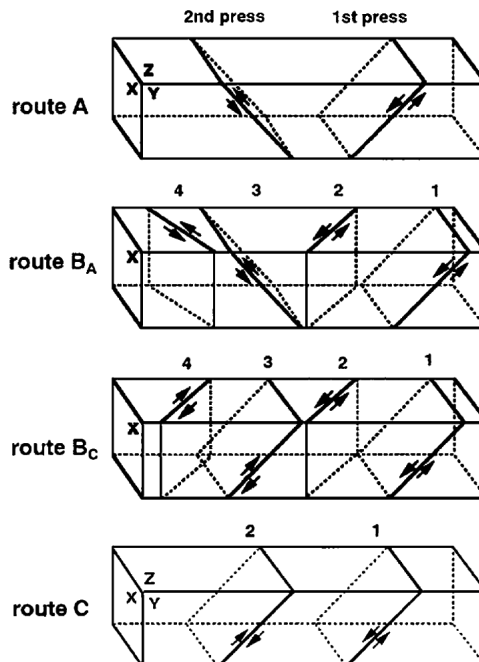


Figure 1.5: The activated slip systems in X, Y and Z planes in ECAP using routes A, B_A, B_C and C [54].

The channel angle Φ is one of the most important ECAP parameter mainly because it determines the strain imposed during pressing. The influence of the channel angle was studied on pure aluminum using a series of ECAP dies with different values of Φ (90° - 157.5°) [55]. Several samples with the same imposed strain were produced in different dies, whereas the number of passes increased with increasing channel angle. Nakashima et al. demonstrated that the microstructure becomes less regular and that the higher fraction of low angle grain boundaries is formed with increasing Φ . The total strain was therefore not the decisive factor for the microstructure development. ECAP dies with the channel angle smaller than 90° are commonly not used because significantly higher pressure is necessary to produce specimens without cracks.

Another parameter that can influence the microstructure is the pressing speed. The influence of the pressing speed was investigated by Berbon who did not observe any significant influence on the average grain sizes [47]. However, it was demonstrated that more equilibrated microstructure is produced by lower pressing speeds. On the other hand, recrystallization may occur due to extended exposure of the specimen to the processing temperature in the die. This effect is obviously suppressed at higher temperatures. In these cases, however, the microstructure becomes coarser.

The pressing temperature is a crucial parameter in ECAP. Extensive investigation was made in this regard, e.g. [56, 57], and several significant trends were observed. Firstly, the average grain size increases with increasing pressing temperature (see Fig. 1.6). Secondly, the fraction of high-angle grain boundaries and the crack density decreases with increasing temperature. Therefore, the fraction of high-angle grain boundaries and the crack density increases with decreasing temperature. However, if we want to achieve material with high fraction of high-angle grain boundaries and with low crack density, the optimal pressing temperature has to be found.

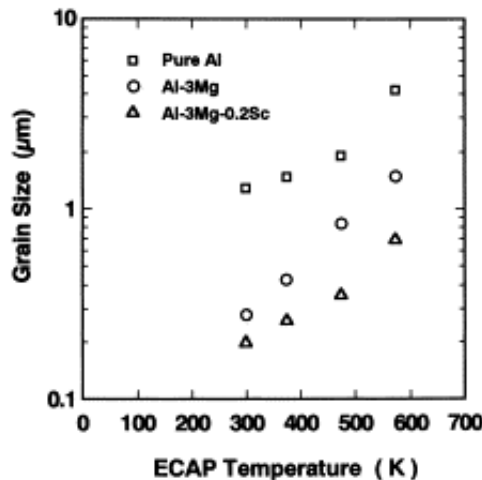


Figure 1.6: The average grain size after ECAP as a function of the pressing temperature for pure aluminum and two different aluminum alloys [56].

Another important parameter which influences the final microstructure of ECAPed specimen is the back-pressure. In this case, the pressure is applied in the exit channel

of ECAP die in the opposite direction to the movement of the pressed billet, see Fig. 1.7. The use of back-pressure leads to a significant improvement in the workability of processed billets which allows to increase the number of passes and to reduce crack formation [58]. Moreover, the samples processed by ECAP without a back-pressure have less homogenous microstructure in the area close to the bottom surface of the billet. Back-pressure also positively influences the grain refinement [59]. Xu et al. showed that in commercial AZ31 magnesium alloy the use of back-pressure reduces the average grain size.

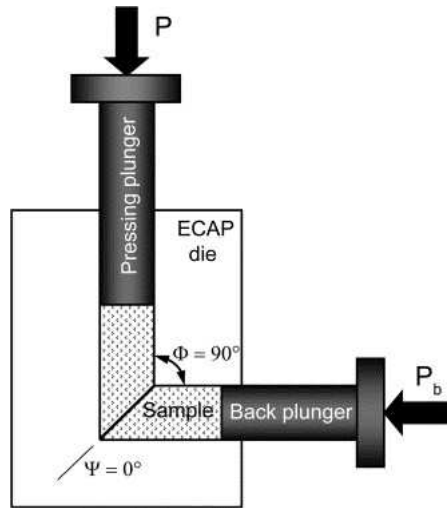


Figure 1.7: Schematic illustration of ECAP die with back-pressure P_b [60]

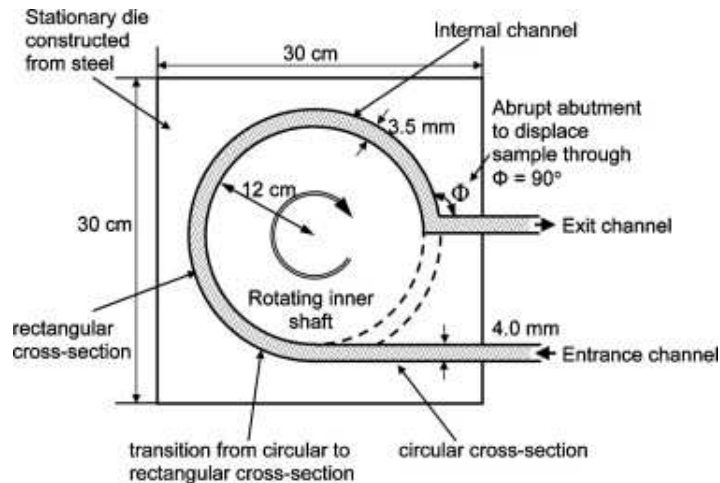


Figure 1.8: Schematic illustration of conform ECAP die [61]

Conventional ECAP has also several disadvantages. The limited specimen dimensions were already mentioned. The main disadvantage is that the conventional ECAP is a discontinuous process, which consists of the repetitive sequence of pressings through the die, removing and reinserting the sample to impose higher strain. Such a procedure may be used in laboratory research but it is completely inadaptable

for industrial applications. Conform ECAP provides a solution for industrial production of ECAPed material. The principle of this method is schematically shown in Fig. 1.8. The device consists of a rotating inner shaft and an outer stationary die. The specimen enters the die, rotates with the shaft and moves into a groove having a rectangular cross-section. When the material is pressed from the internal to exit channel it is turned through an angle. This angle designated Φ is in this case equal to 90° . The equivalent strain ϵ after one pass in the conform ECAP with $\Psi = 90^\circ$ is close to ~ 1 [61].

1.2.2 High Pressure Torsion

High pressure torsion (HPT) is another severe plastic deformation technique. In this method, the mechanical properties of a material are improved by a high pressure and concurrent torsional straining [26]. HPT was for the first time applied to metals in Russia in 1980s [25].

High pressure torsion mechanism is schematically illustrated in Fig. 1.9. The typical size of the sample is in the order of mm and the thickness is about 0.6 mm. A disc sample is placed between two anvils where it is subjected to a compressive pressure of several GPa. Simultaneously, the lower anvil rotates and the torsional strain is imposed to the sample. The total strain imposed by HPT in the sample can be expressed [62]

$$\epsilon = \ln \left(\frac{2\pi N r h_0}{h^2} \right), \quad (1.3)$$

where N is the number of rotations, r represents the radius of the sample and h_0 and h its initial and final thickness, respectively. In general, it was found that an applied pressure of ~ 5 GPa and more than 5 revolutions of the sample in torsion may produce a sample with a reasonably fine microstructure [63, 64].

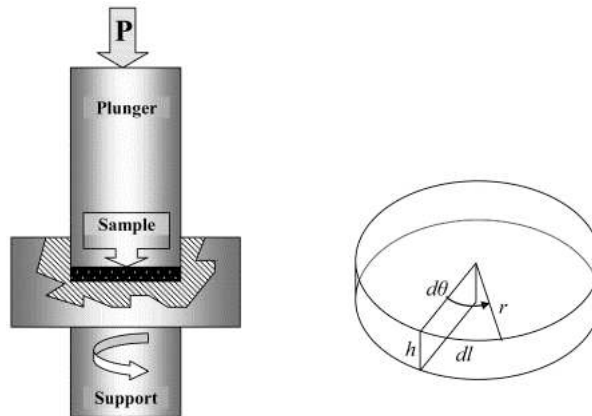


Figure 1.9: Schematic illustration of HPT technique and the parameters of the sample: r is the radius and h is the thickness [65]

Horita et al. showed that high-pressure torsion is more effective than ECAP in producing extremely small grain sizes [66, 67]. Due to an inhomogeneous strain introduced to the specimen by torsional straining an inhomogeneous microstructural refinement occurs. As a consequence the average grain size and mechanical properties

differs across the cross-section of the sample. It was shown that the strain inhomogeneity is reduced by increasing number of rotations [65]. After at least 5 or 8 rotations (depending on material) almost homogeneous strain distribution was observed by several authors [65, 68] who measured microhardness profiles through the specimen cross-section. On the other hand, this apparent disadvantage is eliminated when ring samples are used [69].

However, the small size of the samples is the main disadvantage of HPT method for applications in industry. Because of this limitation, material achieved by this method is used mostly in modern micro-size specialized industrial branches. This technique was successfully employed to several materials, e.g. pure nickel [65] or pure aluminum [69].

1.2.3 Accumulative Roll-Bonding

Accumulative roll-bonding (ARB) is another technique for producing UFG materials. It was invented in Japan in 1990s [27]. The principle of this method is schematically illustrated in Fig. 1.10. In the first step, the strip of a material is rolled to 50 percent reduction of thickness. Subsequently, the strip is cut in two halves and one strip is placed on the top of the second one. Finally, these two strips of material are joined together by rolling. This cycle can be repeated again and again and the strain is accumulated in the material with almost no changes in its dimensions. The equivalent plastic strain ϵ imposed by ARB can be expressed [27]

$$\epsilon = \left\{ \frac{2}{\sqrt{3}} \ln \left(\frac{1}{2} \right) \right\} \times n = 0.80n, \quad (1.4)$$

where n is number of cycles.

The rolling temperature is an important parameter. The rolling force declines with increasing temperature. But the temperature cannot exceed the recrystallization temperature because the imposed strain in material drops due to recrystallization.

Nevertheless, it is possible to apply ARB at room temperature [70]. The microstructure of the material produced by ARB is not equiaxed but comprises a high fraction of high-angle grain boundaries (HAGBs). The limitation of this technique is crack formation near sheet edges especially at higher cycles [71]. On the other hand, the advantage of ARB is that a conventional rolling mill can be used for this method. Therefore, accumulative roll-bonding is a suitable technique for industrial production.

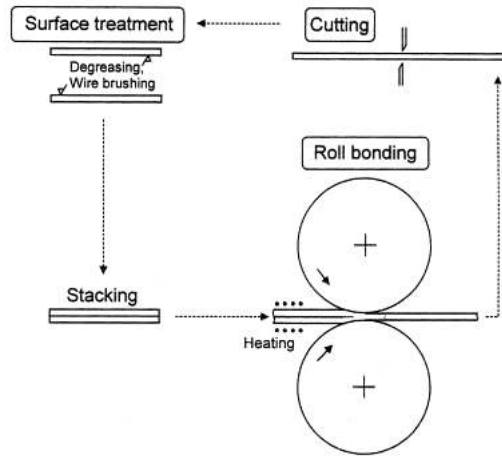


Figure 1.10: Schematic illustration of ARB process [27]

1.3 Important properties of UFG materials processed by SPD

Attainable grain sizes in pure metals processed by SPD techniques vary approximately between 150 and 300 nm. The grains in metal alloys may have even smaller sizes [72]. The microstructure of ultra-fine grained (UFG) materials is complicated and the grain size is not the only one characteristic feature. The homogeneous and equiaxed microstructure, high fraction of high-angle grain boundaries and non-equilibrium grain boundaries with high extrinsic dislocation and vacancy densities are some of the other important properties [73].

The microstructure evolution in UFG materials processed by SPD is not fully understood. Lapovok et al. mean that the microstructure is correlated with the recrystallization in-situ [74], the others interpret the microstructure as a cell dislocation structure [75, 76]. The dislocation cell sizes decrease with increasing strain imposed by SPD. The dislocation cell structure is subsequently transformed to UFG structure. However, the satisfying consistent model describing UFG structure evolution is still not developed.

UFG materials offer generally very good mechanical properties. The unusual combination of high strength and high ductility is one of the significant features typical for UFG materials. This fact was first observed in fine-grained copper and titanium and later proved in many other metals and alloys processed by SPD [77, 78]. This behaviour is caused by the non-equilibrium grain boundaries, bimodal grain size distribution or the presence of nano-size particles of another phase. These results led to the new deformation mechanism discovery in UFG materials, e.g. grain boundary shear at low temperatures [79]. High fatigue limit and fracture toughness belong to the other significant properties of UFG materials [80].

The superplastic behaviour at high rates and low temperature offers interesting industrial application - fast superplastic component forming in automotive or aircraft industry [81]. However, not only mechanical properties are studied in UFG materials processed by SPD. Some UFG materials are multifunctional - for example nano-crystalline TiNi has significant mechanical (superplasticity) and functional (shape

memory) properties [82]. It is known that enlargement of the area of grain boundaries during SPD may lead to the improvement of any kinetic properties of metals. Skripnyuk et al. measured that the kinetics of hydrogen absorption and desorption in magnesium alloy ZK60 can be accelerated by SPD, in their case ECAP [83]. This knowledge offers environment improvements - for example ecological hydrogen-powered automobiles could have blocks of metals as a tank instead of potentially dangerous pressure bottles.

2 Aims of the thesis

The motivation for this research was the extension of current knowledge of physical properties of ultra-fine grained (UFG) materials processed by severe plastic deformation (SPD).

The magnesium alloy AZ31 is well known material and has found a wide range of commercial applications. SPD processes result in strong grain refinement. In addition to small grain size, high fraction of high-angle grain boundaries, homogeneous and equiaxed microstructure, the UFG magnesium alloys exhibit several unique physical properties.

The principal aim of the present work is to study the influence of the number of ECAP passes on the microstructural characteristics of the processed material and to optimize the conditions and number of ECAP passes in order to achieve optimum mechanical and corrosion properties of studied UFG magnesium alloy AZ31.

Physical properties of UFG AZ31 polycrystals are studied by the following experimental techniques:

- mechanical properties by microhardness measurements and tensile tests,
- microstructure development by light and transmission electron microscopy,
- defect structure evolution by positron annihilation spectroscopy,
- texture and microstructure evolution by EBSD measurement,
- corrosion properties by electrochemical impedance spectroscopy.

3 Experimental Procedures

3.1 Experimental material

The commercial magnesium alloy AZ31 was used in this investigation. Its nominal chemical composition is shown in Table 3.1.

Chem. element	Al	Zn	Mn	Mg
Composition [wt. %]	3	0,8	0,2	96

Table 3.1: Nominal chemical composition of alloy AZ31

An equilibrium phase diagram for the binary system AlMg is shown in Fig. 3.1. The right part of the diagram is relevant for our investigation as the alloy AZ31 contains 96 percent of magnesium. Phase δ is a substitutional solid solution of aluminum in magnesium. Phase γ is an equilibrium phase of $Mg_{17}Al_{12}$. The part of the diagram labeled as $\gamma + \delta$ contains mechanical mixture of γ and δ phases.

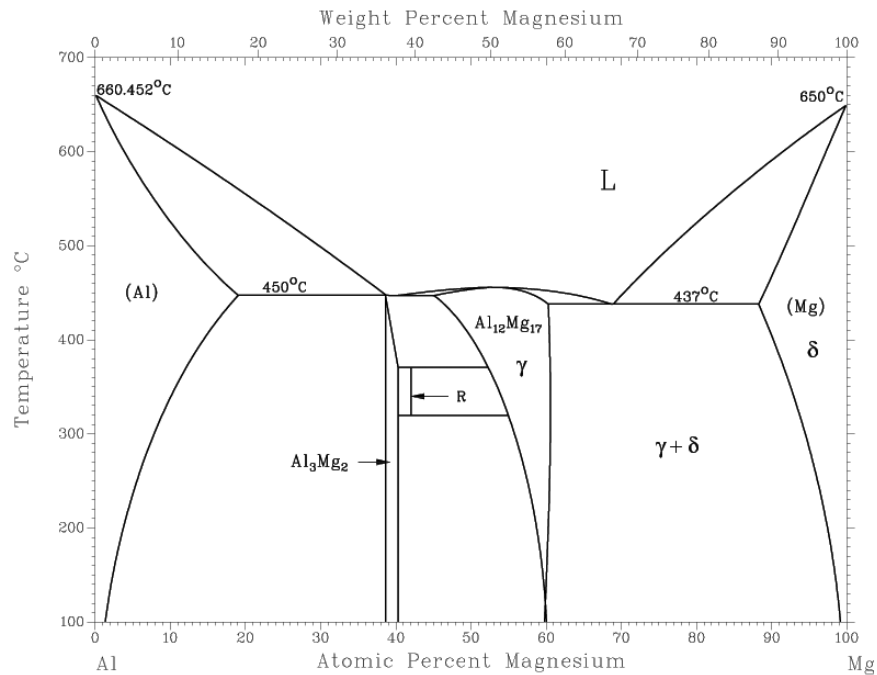


Figure 3.1: A phase diagram of a binary system AlMg [84]

It is well-known, that the properties of ECAPed cast AZ31 alloy are inferior to those prepared by a combined technique comprising the hot extrusion followed by the ECAP. This technique is known as EX-ECAP. In our case the as-cast material was extruded at 350 °C using the extrusion ratio of 22. The ECAP conditions needed to be optimized to obtain compact specimens without surface cracking. After several unsuccessful pressing experiments the following optimum conditions were found: temperature 180 °C,

pressing speed 50 mm/min, MoSi lubricant. The billets were ECAPed using route B_C and number of passes was varied between 1 and 12.

3.2 Light microscopy

The specimen surface for light microscopy observation needs to be plain without impurities or scratches. Polypropylene was used for mounting of specimens for better manipulation. Mounted specimens were prepared by three consequent procedures: mechanical grinding, polishing and etching.

In the first step, the specimens were mechanically grinded on watered abrasive papers. Then the specimens were polished on polishing disc of grade 3 and 1 μm . Using this procedure, flat specimens with minimum surface scratches were obtained. Finally, the polished samples were etched by dilute solution of picric acid. The time period of etching has to be optimized to attain the best possible visibility and no artifacts on the surface.

3.3 Microhardness measurements

The microhardness was measured by a Vickers hardness tester Leco M-400-A. The basic principle of Vickers hardness test is to assess the employed material ability to resist plastic deformation. The diamond indenter in the form of a square-based pyramid with the top angle equal to 136° is loaded and applied to a flat surface of the sample. An indentation left in the specimen after the test has a surface area A , which can be determined by the formula

$$A = \frac{d^2}{2\sin(136^\circ/2)}, \quad (3.1)$$

which can be approximated to give

$$A \approx \frac{d^2}{1.8544}, \quad (3.2)$$

where d is the average length of the diagonal left by the indenter ($d = \frac{1}{2}(d_1 + d_2)$). The unit of Vickers hardness is represented by Vickers Pyramid Number (HV). The HV number is determined by the ratio

$$HV = \frac{F}{A} \approx \frac{1,854F}{d^2}, \quad (3.3)$$

where F is the force applied to the indenter in kilograms-force and A is the surface area of the indentation in square millimeters.

A load of 100g and the indentation time of 10 s were used in our experiments.

3.4 Tensile tests

Mechanical properties of materials are investigated by various techniques. One of the mostly used tests is the tensile test. Characteristic mechanical values, e.g the yield stress, the tensile strength, elongation to failure may be obtained in a tensile straining of a specimen. During the tensile test the specimen is pulled usually at a constant strain rate and its response to straining is detected by a load cell.

ECAPed billets were cut by a diamond saw into parallel slices of the thickness of 1 mm parallel to the Y-plane. Specimens for tensile tests were machined from the individual slices. Tensile tests were performed at room temperature at the commercial deformation machine Instron 8850.

During the tensile test, the applied force F and the elongation Δl are measured. The relative elongation e is theoretically defined as

$$e = \frac{\Delta l}{l_0}, \quad (3.4)$$

where l_0 and Δl is the initial sample length and the elongation, respectively. The elongation is determined from the cross-head speed v and the duration of the test t_i

$$\Delta l(t_i) = vt_i. \quad (3.5)$$

The initial elastic deformation of the specimen and the machine has to be subtracted from the measured elongation Δl . Denoting α and β the y-axis offset and the slope of the linear part of $F - \Delta l$ curve, respectively, the elongation is more precisely expressed by

$$e = \frac{\Delta l + \frac{\alpha}{\beta}}{l_0}. \quad (3.6)$$

True stress σ is defined as

$$\sigma = \frac{F}{S_0}(1 + e), \quad (3.7)$$

where S_0 is the initial cross-section of the specimen. The response of the specimen to the plastic deformation is represented in terms of the stress-strain curve. The true strain ϵ is defined as [85]

$$\epsilon = \int_{l_0}^l \frac{dl}{l} = \ln(1 + e). \quad (3.8)$$

True plastic strain ϵ_p can be calculated from (3.6) and (3.8) and by subtracting elastic deformation as

$$\epsilon_p = \ln \left(1 + \frac{\Delta l + \frac{\alpha}{\beta} - \frac{F}{\beta}}{l_0} \right). \quad (3.9)$$

Two characteristic points can be evaluated from the stress-strain curve, in particular, the yield stress $\sigma_{0.2}$ and the tensile strength σ_{max} . The yield stress $\sigma_{0.2}$

is defined as the true stress where a true plastic strain is equal to 0.2%. The tensile strength σ_{max} is defined as a maximum of the true stress. In engineering practice it is common to refer to ultimate tensile strength (UTS) as

$$UTS = \frac{F_{max}}{S_0}. \quad (3.10)$$

3.5 Positron annihilation spectroscopy

Positron annihilation spectroscopy (PAS) is a non-destructive spectroscopy technique to study the defect structure in solids. The PAS method is based on the fact that a positron which meets an electron annihilates. Gamma photons are emitted as a result of the positron-electron annihilation and are detected by the PAS detector. If the positron moves in the area of high electron density the probability to meet an electron is high and its lifetime is much shorter than in the opposite case when almost no electrons are present in the lattice. The probability $N(t)$ that a positron is still alive at a given time t is

$$N(t) = e^{-\lambda t}, \quad (3.11)$$

where λ is a positron annihilation rate and $N(0) = 1$. Free positron lifetime τ is defined as

$$\tau = \frac{1}{\lambda}. \quad (3.12)$$

Positron lifetime spectrum is defined as

$$-\frac{N(t)}{dt} = \lambda e^{-\lambda t}. \quad (3.13)$$

Positron lifetime spectrum is measured in a positron-lifetime spectrometer. The spectrometer consists of a radioactive source (^{22}Na), and a start and a stop detector. Positron is emitted by the source and propagates in the sample. In a defect free lattice positron is delocalized and may be described by a wave function. If some lattice defect exists in the solid it behaves like a potential well. In this case the wave function is localized in the vicinity of the defect, the positron is trapped there and its lifetime is therefore longer. As a consequence, positron lifetime correlate with the density of individual lattice defects.

In order to attain uniquely determined free positron lifetimes the source of positrons has to be weak and the detector dead time very short. By decomposition of positron lifetime spectra information about individual defect density in the investigated material may be obtained. The defects type may be determined from the lifetimes τ_i while the defect densities are proportional to PAS intensities I_i .

3.6 EBSD

Electron backscattered diffraction (EBSD) is a microstructural crystallographic technique for the determination of crystallographic orientation. Texture, grain size and distribution,

the misorientation of individual grains, the types of grain boundaries and many other microstructural features may be obtained from EBSD results.

The scanning electron microscope (SEM) equipped with the back-scatter detector was used for EBSD investigation of the microstructure and its evolution in individual specimens after ECAP. A field emission gun (FEG) of a Schottky type was used as a source of electrons in the microscope. Beam voltage in the range from 200 V to 30 kV is applicable. The acceleration voltage employed was 15 kV.

The samples for EBSD investigation were first mechanically grinded on watered abrasive papers of grade 600, 800 and 1200. Then the specimens were mechanically polished to $0.3 \mu\text{m}$ with Al_2O_3 . The final electrolytical polishing using a Gatan PECS device and Struers-AC2 electrolyte at the temperature of $-20 \text{ }^\circ\text{C}$ was used to remove the surface layer influenced by polishing. Finally a short etching was applied to reveal the grain structure. The EBSD measurements were conducted at the mid-area of the cross sectional planes of the extruded and ECAPed samples.

During the automatized step by step measurement, the accelerated high energy electrons interact with the atomic lattice of the crystalline material and form so called Kikuchi lines on the screen. The formation of Kikuchi lines is caused by inelastic electron scattering. The inelastically scattered electron wave length is slightly longer than the wave length of elastically scattered electrons and the inelastic scattered electron intensity decreases with increasing scattering angle. In certain crystal orientations some planes satisfy the Bragg condition (with diffraction angle θ) and the inelastically scattered electrons are Bragg diffracted. These electrons are called Kikuchi electrons. Kikuchi electrons move along conical surfaces whose top angle is equal $(\pi - 2\theta)$ and the axis of diffraction planes is the normal line. Two hyperbolas are formed by the intersection of the conical surfaces and a screen. The hyperbolas seem like straight lines in the central part of diffractogram and the distance between lines corresponds to the angle 2θ .

3.7 Transmission electron microscopy

Transmission electron microscopy (TEM) is a technique that study the microstructure of the material using a beam of high energy electrons. The specimens for TEM have to be very thin (100 - 200 nm depending on the acceleration voltage). An image is formed from the interaction of the specimen with the transmitted electrons and focused on a fluorescent screen or a photographic film.

The sample preparation consists of two steps - mechanical thinning and polishing. The type of polishing depends on the physical and chemical properties of the material.

In our case the ECAPed billets were first cut into slices of the thickness of 1 mm. The slices were mechanically grinded from both sides to the thickness of $100 \mu\text{m}$. The 3 mm diameter disks were cut out of the thin slices and dimpled from one side to the thickness cca $30 \mu\text{m}$ (see Fig. 3.2). This dimpling technique reduces ion polishing times.

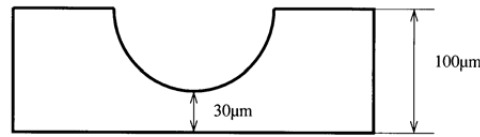


Figure 3.2: Schematic illustration of the specimen after dimpling [86]

Ion polishing is used for materials which cannot be polished electrolytically. Ion polishing is a method for removing very fine quantities of the material. It uses an inert gas (argon) to generate a plasma stream that is emitted to the thinned area of the sample and removes the individual layers of the material. Acceleration energies vary usually from 4 to 6 keV. Ion beam always enters the sample. The penetration depth depends on the angle between a direction of the ion beam and the sample surface. The angle of incidence is usually less than 5° .

The Precision Ion-Polishing System (PIPS) schematically shown in Fig. 3.3 was used for final preparation of thin foils for TEM. The polishing apparatus consists of two ion guns located on the opposite sides of the device. The ion beams emitted from the guns are accelerated and focused on the rotating specimen disk. The optimum conditions found were following: the acceleration voltage of 4 kV, the angle of incidence of 5° and room temperature. In the final stage the acceleration voltage is reduced to 2 kV and the angle of incidence to 2° . The specimen preparation for transmission electron microscopy is finished when a small hole is formed in the sample and the surrounding area is thin enough to allow high energy electrons to pass through the specimen.

The microstructure observation was made with the TEM JEOL 2000FX in Prague and TEM Philips CM 200 at the Technical University in Clausthal. The applied accelerated voltage was 200 kV in both cases.

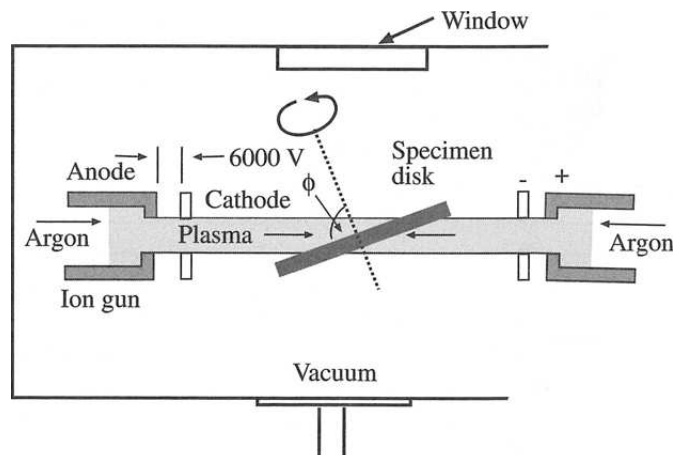


Figure 3.3: Schematic illustration of device for ion polishing (PIPS) [87]

3.8 Corrosion tests

Corrosion properties are one of the most important properties that influence industrial and constructional applicability of materials. Several standardized corrosion tests are developed and employed. The electrochemical corrosion tests are the most common tests - the electrochemical characteristics are determined from measuring of a potential and a current density, or measuring of a corrosion system impedance. The electrochemical corrosion methods include potentiodynamic, potentiostatic, galvanostatic, electrochemical impedance spectroscopy, etc. In a potentiodynamic method the dependence of a current density on the potential of the investigated specimen is measured and compared with a referential electrode.

The electrochemical impedance spectroscopy (EIS) is a method applicable for samples with non-conducting or weak-conducting surface layer. The alternating voltage is applied in an electrical circuit and the impedance is measured in the frequency range from hundreds of kHz to mHz. The measuring device for EIS consists of the electrolyte container, the measuring instrument, the computer and three electrodes: auxiliary, referential and working electrode. The EIS is a very sensitive technique but it does not provide a direct characteristics of the physical phenomena. An appropriate choice of a model is required to interpret the data. The real sample surface is equivalent to a set of circuit elements - in particular resistances and capacitors.

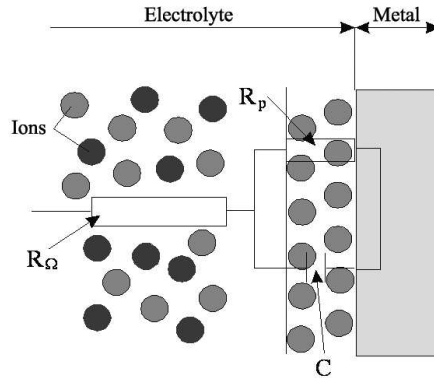


Figure 3.4: The equivalent circuit of the interface between the metal and the electrolyte

The simplest case is shown in Fig. 3.4. This model of the interface between the metal and the electrolyte consists of an equivalent circuit with a resistance R_Ω (the electrolyte resistance) and parallel-connected resistance R_p and capacitor C (the resistance and capacitance of an electric layer between the sample and electrolyte). The formula for the impedance of the equivalent circuit is:

$$Z = R_\Omega + \frac{R_p \frac{1}{i\omega C}}{R_p + \frac{1}{i\omega C}}. \quad (3.14)$$

The complex impedance Z may be expressed as a sum of the real and imaginary term

$$Z = R_\Omega + \frac{R_p^2}{(\omega C R_p)^2 + 1} - i \frac{\omega C R_p^2}{(\omega C R_p)^2 + 1}. \quad (3.15)$$

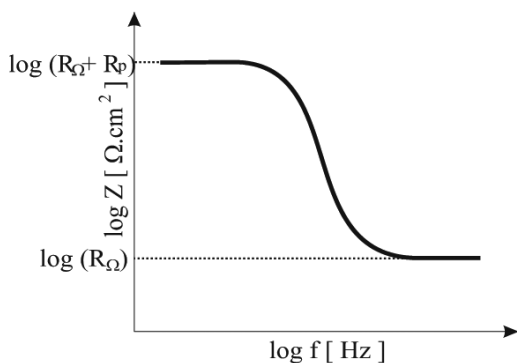


Figure 3.5: The logarithmic frequency characteristic

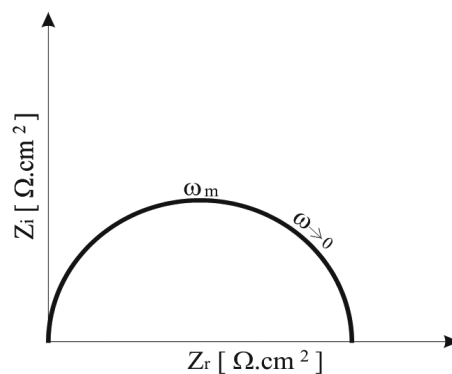


Figure 3.6: The Nyquist diagram

Measured data are depicted in the logarithmic frequency characteristic (see Fig 3.5) or Nyquist diagram (see Fig 3.6). More complicated models describe, for example, corroding specimens with two layers or a porous layer and contain an equivalent circuit with more circuit elements. In these cases, the logarithmic frequent characteristics and the Niquist diagrams are different and more complicated. Models may be fitted to the measured data allowing to obtain magnitudes of all elements in the equivalent circuit.

The corrosion tests were done at the University of Žilina. The ECAPed billets were cut into slices of the thickness of 3 mm. The slices were mounted with polypropylen, mechanically grinded on abrasive paper of grade 1200 and degreased with toluene. The measuring device Voltalab 10 - PGZ 100 is controlled by the program VoltaMaster 4. The working electrode contains a rotary head which allows to remove gas bubbles which form during the oxidation. The auxiliary electrode is composed of platinum and a saturated calomel electrode is used as the referential electrode. The solution of 0.1M NaCl was used as the electrolyte.

4 Experimental results and discussion

4.1 Microstructure after ECAP

The microstructure evolution of extruded specimens processed by different number of ECAP passes is shown in this section. The extruded sample microstructure is shown in Fig. 4.1. The sample consists of two types of grains - large grains and the amount of small grains. The microstructure developed only slightly after the first and the second ECAP pass, the bimodal structure is still observed, see Fig. 4.2. The microstructure changes begin to be significant in light microscopy after 4 ECAP passes. One can see in Fig. 4.3 that the large grains become smaller. However, the bimodal structure is no more observed after 8 and 12 ECAP passes. The homogeneous microstructure of this sample is shown in Fig. 4.4.

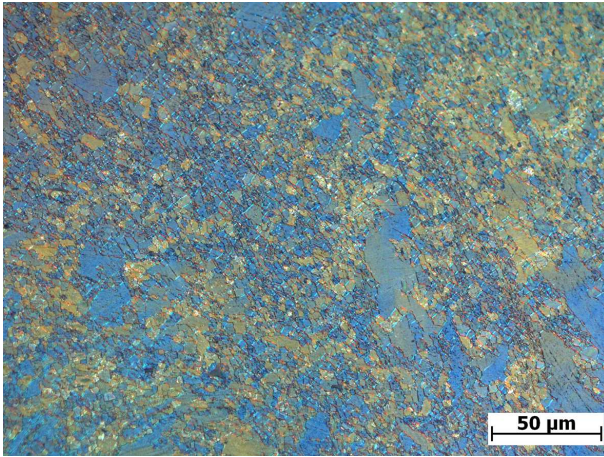


Figure 4.1: The X-plane of the extruded sample (0P)

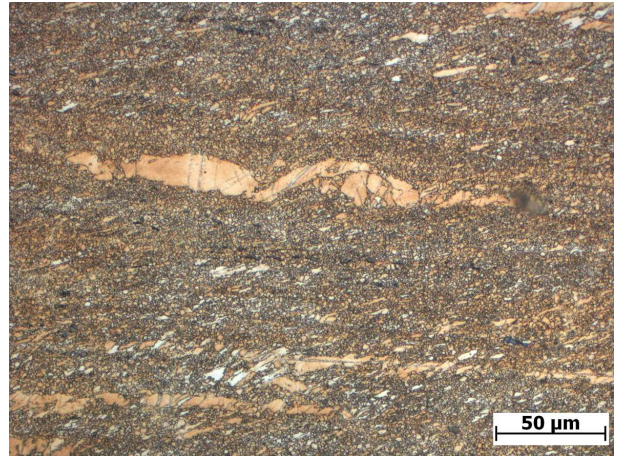


Figure 4.2: The Y-plane of the extruded sample after 2 ECAP passes (2P)

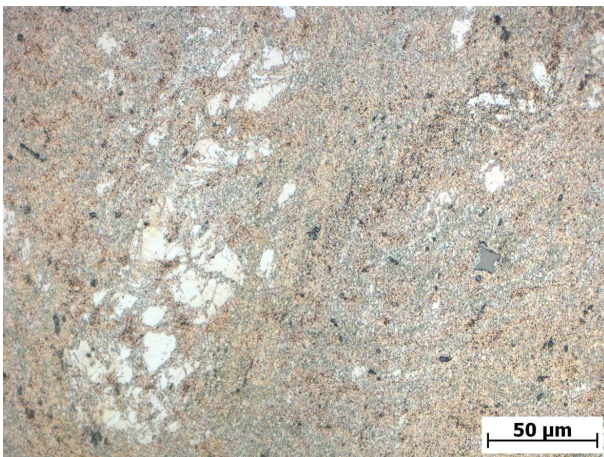


Figure 4.3: The X-plane of the extruded sample after 4 ECAP passes (4P)



Figure 4.4: The X-plane of the extruded sample after 12 ECAP passes (12P)

4.2 Mechanical properties

4.2.1 Microhardness

The microhardness of all samples was measured on all three reference planes. The indenter was applied minimally ten times in each test. The indentations were located in a central part of the sample in a line perpendicular to the specimen edge. The first indentation was situated in the distance of 0.5 mm from the edge and the following ones were successively made at the same distance along a line. The microhardness values were calculated from the indentation parameters using the program Lucia Hardness and are summarized in Tab. 4.1.

In Tab. 4.1 we can see that the microhardness is markedly higher after the first ECAP pass. The microhardness increases only slightly up to the fourth pass and then declines up to the twelfth pass. No statistically significant differences of microhardness in individual planes was found.

No. of Passes	HV		
	X	Y	Z
0	69.8 ± 1.9	68.5 ± 1.8	68.5 ± 1.8
1	80.3 ± 3.9	79.3 ± 1.6	80.5 ± 1.2
2	81.6 ± 3.2	82.2 ± 2.2	83.8 ± 1.6
4	85.1 ± 2.9	89.5 ± 1.4	85.2 ± 1.2
8	82.5 ± 1.6	84.3 ± 1.7	83.2 ± 0.7
12	78.7 ± 1.8	81.0 ± 1.9	81.0 ± 3.1

Table 4.1: The microhardness values in individual specimens and various planes

4.2.2 Tensile properties

ECAPed billets were machined and cut by a SiC saw into parallel slices of the thickness of 1 mm parallel to the Y-plane. Tensile tests were performed at room temperature at the commercial deformation machine Instron 5882 using the initial strain rate of $10^{-4} s^{-1}$.

Measured data were processed using OriginPro 7.5. Force-elongation dependence was firstly interpolated and smoothed using moving average process. Linear part was localized manually. Linear fit was computed and elastic part subtracted. True strain, true plastic strain and true stress were counted from linear fit parameters and sample dimensions according to Eq. (3.7),(3.8) and (3.9). As a result, the flow curve (true stress-true strain dependence) was estimated, see Fig. 4.5. The yield stress ($\sigma_{0.2}$) was estimated from the flow curve. Work hardening was calculated by numerical differentiation with smoothing. The magnitude of the yield stress increases slightly up to the second pass and then declines markedly up to the eight pass and slightly to the twelfth pass, see Fig. 4.6.

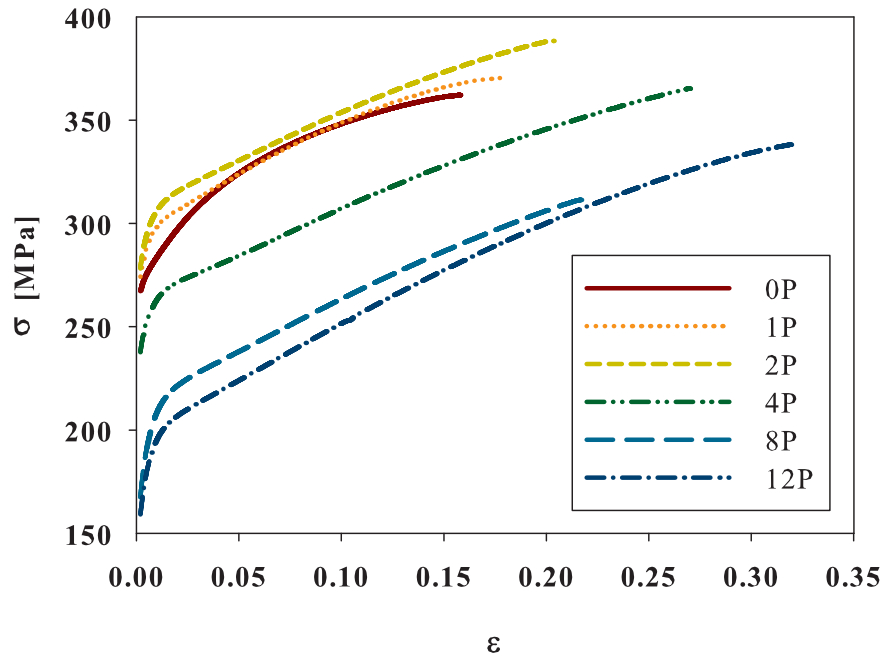


Figure 4.5: Flow curves of extruded specimens processed by different number of ECAP passes

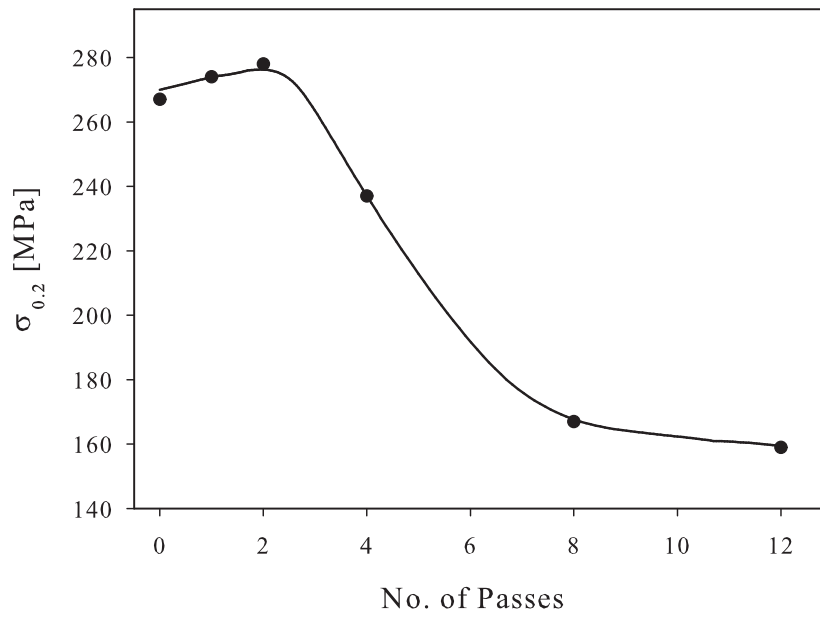


Figure 4.6: The dependence of the magnitude of yield stress on the number of ECAP passes

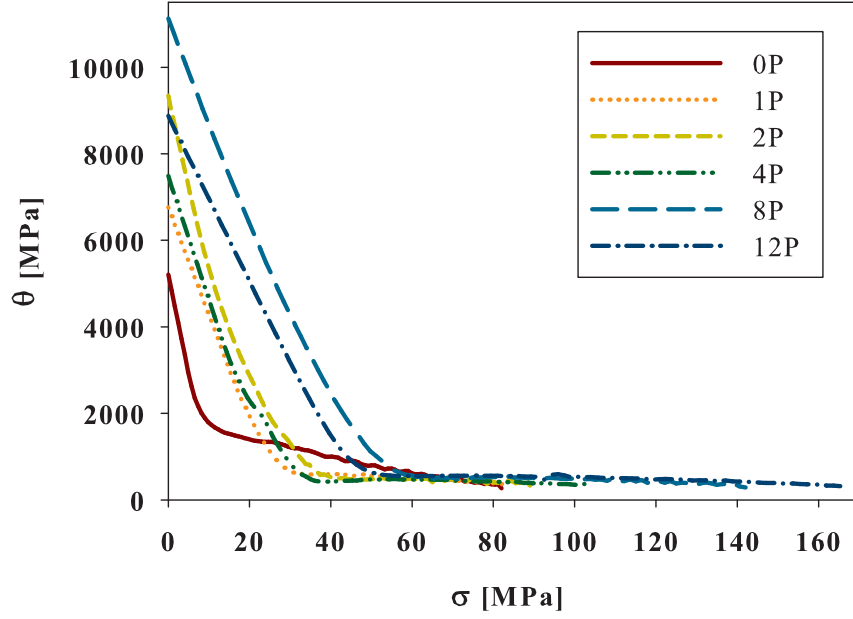


Figure 4.7: Work hardening curves of extruded specimens processed by different number of ECAP passes

Several models attempted to describe stress-strain curve. The first useful equation was developed by Hollomon in the form of an empirical power law

$$\sigma = A\epsilon^D + C. \quad (4.1)$$

Model equation predicts no upper limit on the value of stress. Nevertheless Hollomon model fails to fit experimental data particularly at high strains.

Alternative relationship has been proposed by Voce:

$$\sigma = A - Be^{-C\epsilon}. \quad (4.2)$$

Disregarding the Hollomon model, Voce model assumes the saturation of stress at high strains:

$$\lim_{\epsilon \rightarrow \infty} \sigma = A. \quad (4.3)$$

However, Voce empirical model is not appropriate to describe the whole flow curve. This can be clearly seen from transforming Voce model into work hardening curve

$$\theta = CA - C\sigma. \quad (4.4)$$

Simple linear function obviously does not describe the whole work hardening curve.

These shortcomings are discussed by Chinh et al. [88] and improved phenomenological combination of these two models is developed in the form

$$\sigma = A - Be^{-C\epsilon^D}. \quad (4.5)$$

This equation is referred to as Chinh model. For D being equal to 1, Chinh model is equivalent to Voce equation. Note that Taylor expansion of (4.5) at small strains is identical to Hollomon relationship. Determining Chinh model equation for work hardening is far less illustrative than Voce equation

$$\theta = \frac{d\sigma}{d\epsilon} = (CA - C\sigma) \left(\frac{\ln\left(\frac{B}{A-\sigma}\right)}{C} \right)^{\frac{D-1}{D}}. \quad (4.6)$$

However, even this equation can be fitted into experimental data.

The flow stress of crystalline materials σ depends on the dislocation structure which may be represented by the average dislocation density ρ as follows [88]

$$\sigma = M\alpha Gb\sqrt{\rho} \quad (4.7)$$

where M is a Taylor factor, α is a geometrical constant, G is a shear modulus and b is the magnitude of the Burgers vector. The dislocation structure changes during tensile tests. A part of mobile dislocations is stored, forms subsequently new obstacles for dislocation motion and thus contributes to hardening. On the other hand, dislocations may annihilate which contributes to softening. Kocks [89] assumes that the mean free path of dislocations is proportional to the average dislocation spacing and the change in the dislocation density is due to some recovery. The evolution equation is then given by

$$\frac{d\rho}{d\gamma} = \kappa_f\sqrt{\rho} - \frac{L_{CS}\rho}{b}, \quad (4.8)$$

where L_{CS} is the average length of the dislocation segment recovered in one recovery event, κ_f is a geometrical factor and γ is a shear strain. Using the relationship between the total strain and the shear strain $\epsilon = M^{-1}\gamma$ and the dependence of plastic stress on dislocation density according to (Eq. (4.7)), it can be shown that the work hardening rate follows Voce relationship. Parameters of the Voce model can be theoretically explained employing this Kocks model. However, this model does not allow to describe the whole work hardening curve.

In contrary to Kocks model, model of Estrin and Mecking [90] assumes that the mean free path of dislocations is constant and it is determined by the spacing between impenetrable obstacles. This results in the following evolution equation

$$\frac{d\rho}{d\gamma} = \frac{1}{bs} - \frac{L_{CS}\rho}{b}, \quad (4.9)$$

where s is grain size or partical spacing.

Malygin model [91] takes into account both kinds of obstacles to dislocation motion. The evolution equation has the following form in this case

$$\frac{d\rho}{d\gamma} = \frac{1}{bs} + \kappa_f\sqrt{\rho} - \frac{L_{CS}\rho}{b}. \quad (4.10)$$

The theoretical equation describing the work hardening curve may be derived from the evolution equation (4.10):

$$\theta = \frac{d\sigma}{d\epsilon} = \frac{A}{\sigma - \sigma_y} + B - C(\sigma - \sigma_y), \quad (4.11)$$

where the following substitutions were made:

$$\begin{aligned} A &= \frac{1}{2}M^3(\alpha Gb)^2 \frac{1}{bs}; \\ B &= \frac{1}{2}M^2\alpha Gb\kappa_f; \\ C &= \frac{1}{2}M\frac{LCS}{b}. \end{aligned} \quad (4.12)$$

It can be seen that Malygin work hardening curve consists of three terms. The first term is hyperbolic and as such it plays a crucial role in the beginning of plastic deformation. From definition of parameter A , it should be pointed out that the spacing between impenetrable obstacles plays the key role. The third term on the right side of the equation (4.11) is a linear term that describes constant softening process due to cross-slip.

Fit of both empirical Chinh and theoretical Malygin models are presented in the following graph.

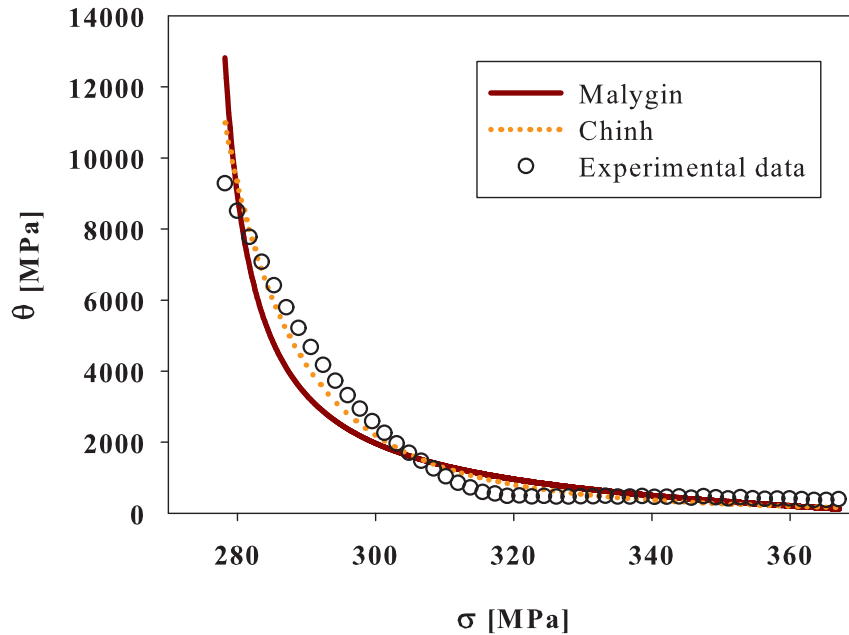


Figure 4.8: Results of fitting of work hardening curve in case of extruded specimen after 2 ECAP passes according to the Malygin and Chinh models

The agreement of both theoretical curves with experimental data is not very satisfactory. The reason is a non-hyperbolic behaviour in the initial part of the work

hardening curve, where the model assumes s (spacing between obstacles) to be constant. This would be true if these obstacles were grain boundaries. In fact, during plastic deformation of magnesium alloy AZ31 twinning can occur. These twins are created continuously at the initial stages of plastic deformation and thus s is no longer constant. As a consequence, the parameter A is no longer constant but depends on strain. As a result, the beginning of work hardening curve does not follow hyperbolic pattern. The deep understanding of twinning process in extruded AZ31 after ECAP goes beyond the scope of this thesis and is the subject of our future research.

The second part of the $\theta - \sigma$ curve was independently fitted by a linear function with the aim to find the parameter C . The results of the fit are summarized in Tab. 4.2.

No. of Passes	Coefficient C
0	18.0
1	5.0
2	2.6
4	2.8
8	3.5
12	3.2

Table 4.2: The magnitudes of slope coefficient C in Malygin model

Parameter C of Malygin model can be rewritten in the form:

$$C = M \frac{cL_{CS}}{2b\rho_{orig}}, \quad (4.13)$$

where c is the area concentration of the recovery sites in a slip plane and ρ_{orig} is the dislocation density in the material before deformation. Experimental values of parameter C can be thus related to positron annihilation spectroscopy measurements of dislocation density (see further).

4.3 Microstructure and defect structure evolution using PAS

Positron lifetime measurements were performed using a fast-fast spectrometer [92] with a timing resolution of 160 ps. At least 10^7 positron annihilation events were accumulated at each positron lifetime spectra which were subsequently decomposed using a maximum likelihood procedure [93].

Coarse grained AZ31 has a single component positron lifetime spectra with comparable lifetimes to free positron lifetime in well annealed magnesium [94]. Thus, the coarse grained alloy contains very low density of defects and almost all positrons are delocalized in the lattice and annihilate from the free-state. Only one short lived free positron component with lifetime τ_1 was measured in the coarse grained material.

On the contrary, positron lifetime spectra of the extruded and ECAPed material exhibit two-component spectra. The second component with lifetime $\tau_2 \approx 260ps$ was measured. This component arises from positrons trapped at dislocations introduced

by extrusion and equal-channel angular pressing. The dependence of lifetimes τ_1 and τ_2 on the number of ECAP passes is shown in Fig. 4.9. The development of relative intensity I_2 of the dislocation component with increasing number of passes is shown in Fig. 4.10. One can see in Fig. 4.9 that lifetime of positrons trapped at dislocations remains approximately constant. The intensity I_2 of positrons trapped at dislocations increases up to the second pass due to the increasing number of dislocations introduced by deformation. The intensity I_2 saturates after the second pass and then decreases with increasing number of passes.

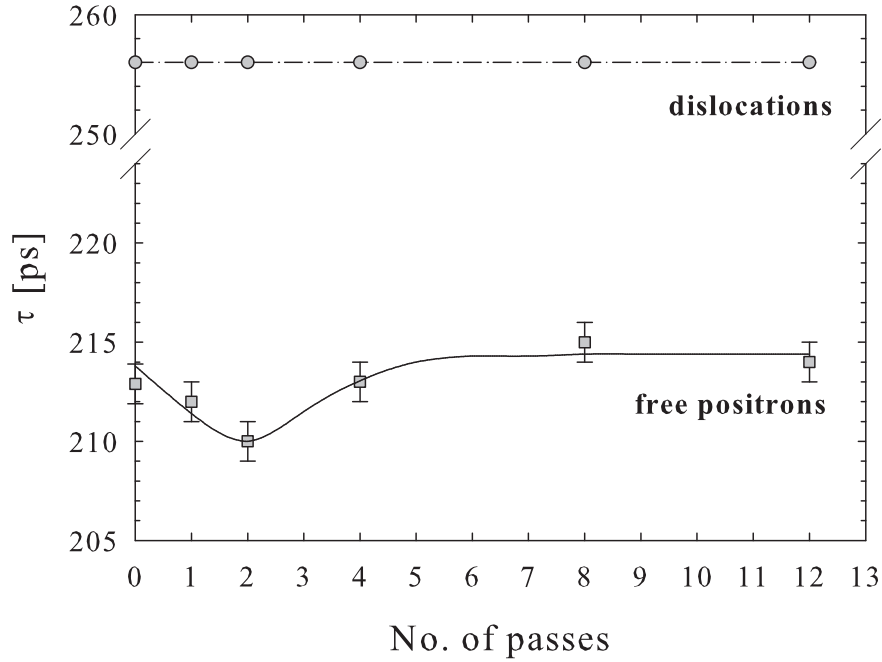


Figure 4.9: Dependence of lifetimes τ_1 and τ_2 on the number of ECAP passes

The mean dislocation density ρ_D can be calculated from positron lifetime data using the two-state simple trapping model [95]

$$\rho_D = \frac{1}{\nu_D} I_2 \left(\frac{1}{\tau_1} - \frac{1}{\tau_2} \right), \quad (4.14)$$

where ν_D is the specific positron trapping rate to dislocations. As a value of the rate was used $\nu_D = 1 \times 10^4 m^2 s^{-1}$ estimated for dislocations in magnesium [96].

In the two-state trapping model, the quantity

$$\tau_f = \left(\frac{I_1}{\tau_1} + \frac{I_2}{\tau_2} \right)^{-1} \quad (4.15)$$

equals to the bulk positron lifetime in defect-free material. The extruded specimens deformed by ECAP fulfil the equation (4.15) and this testifies that these samples contain a single type of defects and that dislocations are distributed homogeneously in the specimens.

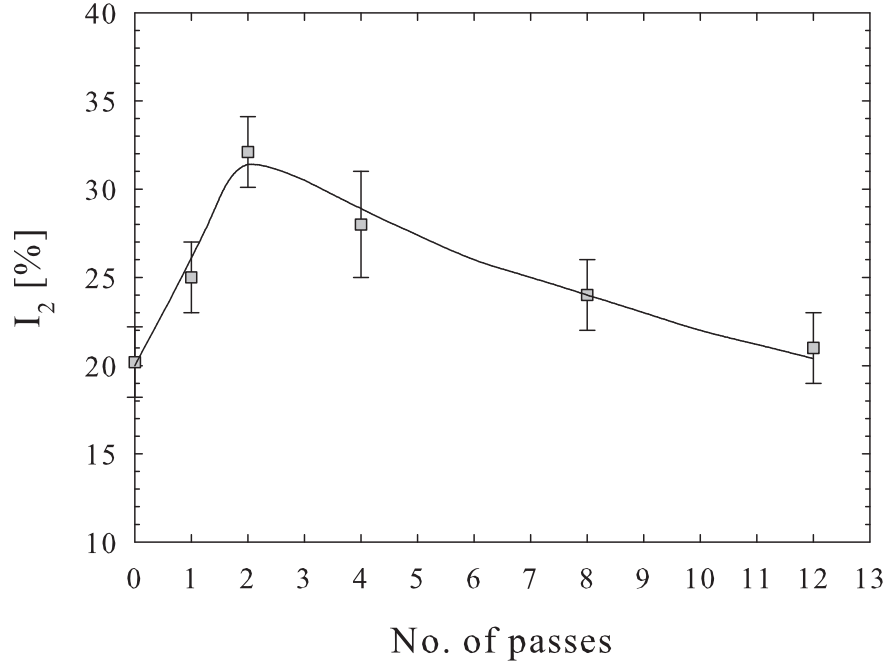


Figure 4.10: Development of relative intensity I_2 of dislocation component with increasing number of ECAP passes

Positron annihilation spectroscopy measurements in the specimens indicate the non-monotonous dependence of the dislocation density on the number of passes. The dislocation density (from Eq. (4.14)) was found to increase up to the second pass and to decline continuously up to the twelfth pass (see Fig 4.11 and Tab. 4.3). This indicates dynamic recovery of dislocations during ECAP processing. These results are in accordance with the results of tensile tests (see Tab. 4.2). The dislocation density is inversely proportional to the slope of the second part of the work hardening curve (see Eq. (4.13)).

No. of Passes	Lifetime [ps]	$\rho_D[10^{12}m^{-2}]$
0	212.9	1.6
1	212.0	2.0
2	210.0	2.7
4	213.0	2.2
8	215.0	1.8
12	214.0	1.6

Table 4.3: The measured lifetime and the dislocation density of extruded specimens after ECAP

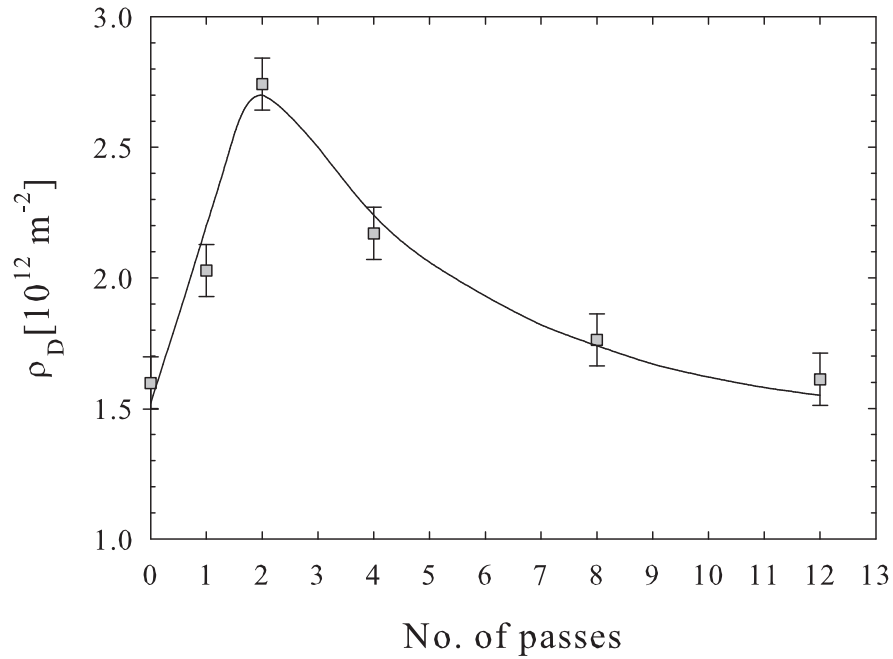


Figure 4.11: Development of dislocation density ρ_D calculated from Eq. (4.14) with increasing number of ECAP passes

4.4 Microstructural characterization using EBSD

The specimens for EBSD measurements were cut from the mid-area of the cross sectional planes (see Fig 4.12) and prepared by the procedure mentioned above. The—microstructure and the texture of the extruded AZ31 alloy is shown in Fig 4.13 in terms of the EBSD inverse pole figure map in the extrusion direction (ED) and the recalculated pole figure using EBSD data. One can see that the microstructure of the extruded specimen is bimodal and consists of large grains of $50 \sim 100 \mu\text{m}$ and relatively fine grains of $2 \sim 5 \mu\text{m}$ around the large ones. Most grains have their crystallographic c-axis perpendicular to the extrusion direction. This fact is typically found in extruded magnesium alloys [97].

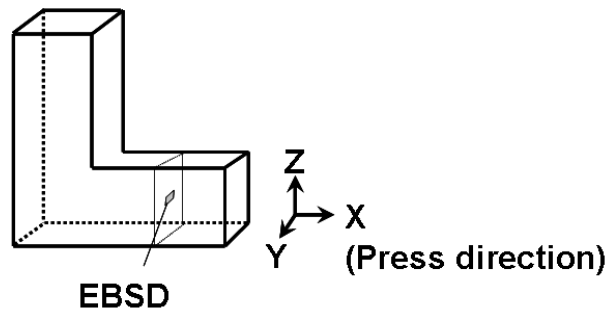


Figure 4.12: The position of samples for EBSD measurements cut from the extruded and ECAPed billets

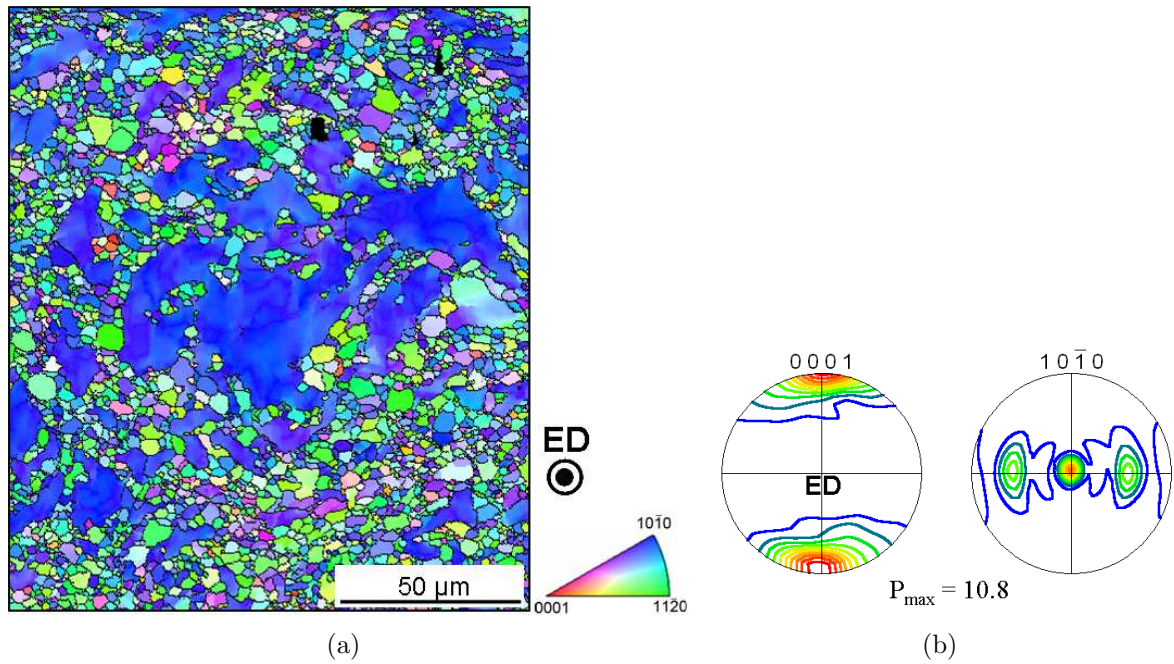


Figure 4.13: (a) EBSD orientation map and (b) recalculated pole figures of the extruded billet. The colour code corresponds to the inverse pole figure in the extrusion direction (ED).

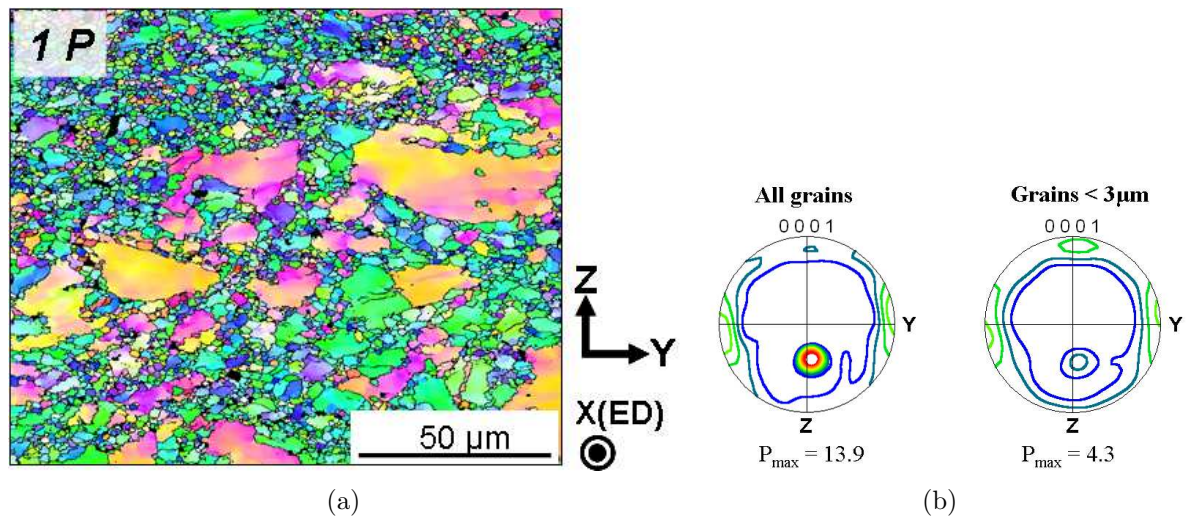


Figure 4.14: (a) EBSD orientation map of the extruded billet after 1 ECAP pass. (b) (0001) pole figure calculated using all grains and (0001) pole figure of grains smaller than $3 \mu\text{m}$.

The microstructure and the texture of extruded specimen after 1 ECAP pass (1P) is shown in Fig. 4.14. The bimodal distribution of grain sizes is still observed in the 1P specimen. As shown in Fig. 4.14 (b), the new texture component is visible in the 1P sample, but mainly in large grains (grain size $> 10 \mu\text{m}$). This component corresponds to the basal poles rotated about 40° from the initial orientation towards the pressing direction and is caused by the shear strain imposed by ECAP [98]. The (0001) pole figure of the grains smaller than $3 \mu\text{m}$ shows that the intensity of the tilted basal poles is rather weak ($P_{max} = 4.3$) in comparison with a pole figure constructed from all grains ($P_{max} = 13.9$). The difference is caused by the fact that the shear strain by the first ECAP pass is mainly accommodated within the large grains. According to the Hall-Petch relation, larger grains are deformed by lower energy comparing to the small grains. The discontinuity of material flow caused by the inhomogeneous deformation seems to be compensated by the occurrence of the dynamic recrystallisation in the vicinity of grain boundaries of large grains, such that the sample could be deformed without failure. The microstructure of the extruded specimen after 2 ECAP passes is very similar to the 1P sample - the distribution of the grain sizes is still bimodal and the orientation of large grains remains almost unchanged.

As shown in Fig. 4.15 (a), the microstructure of the extruded sample after 4 ECAP passes (4P) changes - the amount of the large grains decreases significantly and their sizes became smaller comparing both to the initial and the 1P specimens. Fine grains are formed near the grain boundaries of large grains. This fact indicates that the refinement of the large grains occurs gradually with increasing number of ECAP passes by dynamic rotation recrystallisation mechanism suggested by Ion et al [99]. One can see in Fig. 4.15 (b) that the fine grains (smaller than $3 \mu\text{m}$) in the 4P specimen have mainly the orientation of the rotated basal poles.

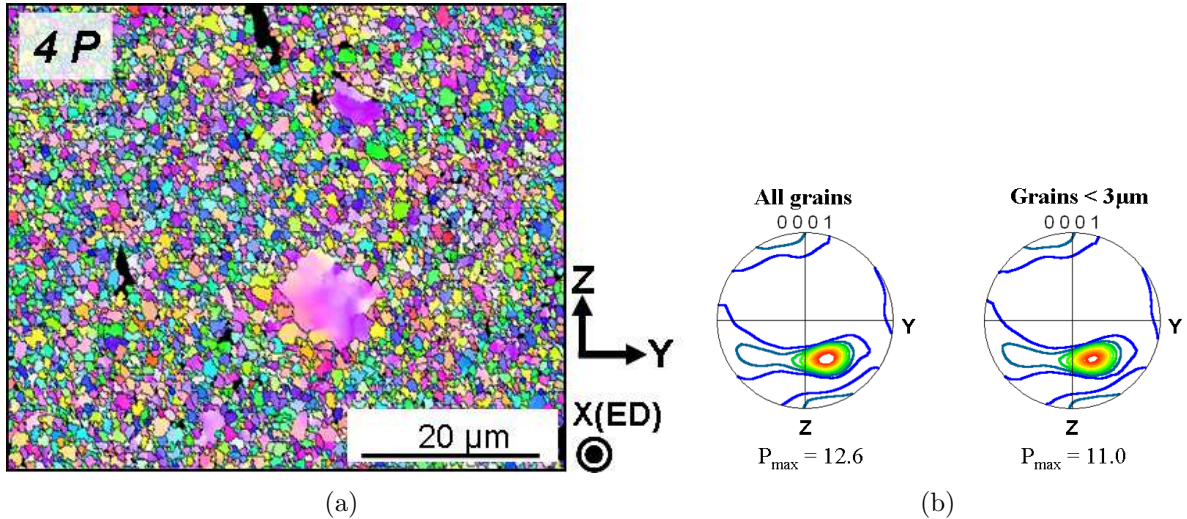


Figure 4.15: (a) EBSD orientation map of the extruded billet after 4 ECAP passes. (b) (0001) pole figure of all grains and (0001) pole figure of grains smaller than $3 \mu\text{m}$.

The microstructure and the texture of extruded specimen after 12 ECAP passes (12P) is shown in Fig. 4.16. The bimodal distribution is replaced by the homogeneous distribution of the fine almost equiaxed grains, no large grains remain in the 12P sample.

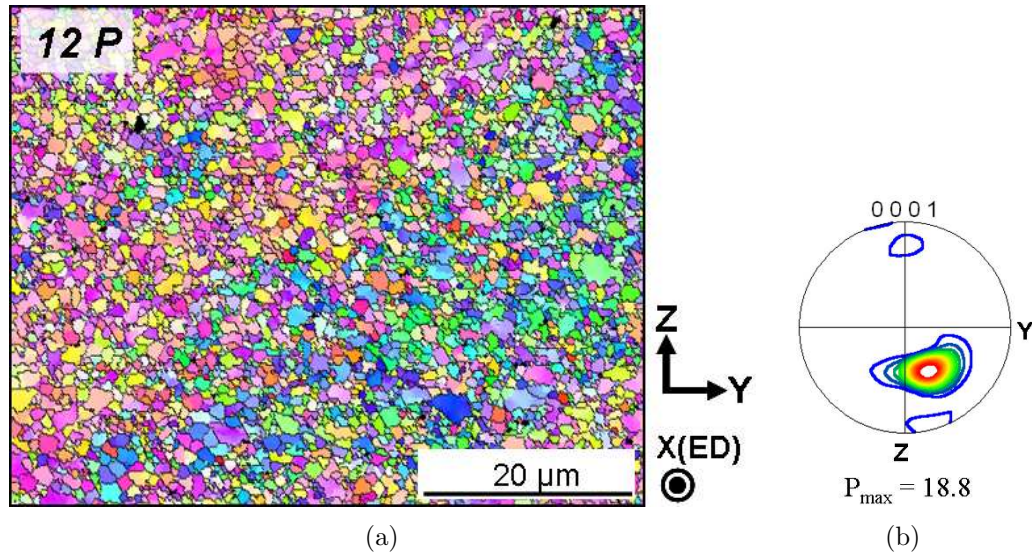


Figure 4.16: (a) EBSD orientation map and (b)(0001) pole figure of the extruded billet after 12 ECAP passes.

As shown in Fig. 4.16 (b), the rotated basal pole became the main texture component.

The grain size distributions of fine grains (smaller than $10 \mu\text{m}$) after different number of ECAP passes is presented in Fig 4.17 (a). The variation in the area fraction of large grains (larger than $10 \mu\text{m}$) is shown in Fig 4.17 (b). The relative fine grains (\sim from 2 to $5 \mu\text{m}$) present in the extruded specimen become finer to $\sim 2 \mu\text{m}$ after the first ECAP pass and the subsequent passes make the grains finer to $\sim 1 \mu\text{m}$. The significant changes are observed in the area fraction of grains larger than $10 \mu\text{m}$, see Tab. 4.4. The area fraction is approximately equal to 18% after the extrusion and remains the same after the first ECAP pass. The area fraction of large grains decreases gradually with additional number of passes until no large grains are observed in the specimens (after 8 ECAP passes).

The variation in the fraction of the low and high angle grain boundaries as a function of the number of ECAP passes is shown in Fig. 4.17 (b). The low angle grain boundary (LAGB) has the misorientation angle smaller than 15° , the high angle grain boundary (HAGB) larger than 15° . The fraction of HAGB decreases after the first ECAP pass from $\sim 70\%$ to $\sim 50\%$, while the fraction increases to $\sim 80\%$ after the second ECAP pass and remains almost unchanged by the subsequent number of ECAP passes. This stabilisation of the HAGB formed by 2 ECAP passes indicates that the dislocations generated by the ECAP did not reach the level necessary for the formation of dislocation cell-structure and further development of HAGB. Because the ECAP was carried out at high temperature the dislocations annihilation process by the dynamic recovery occurred fast enough and the grains could not be further refined after 2 ECAP passes.

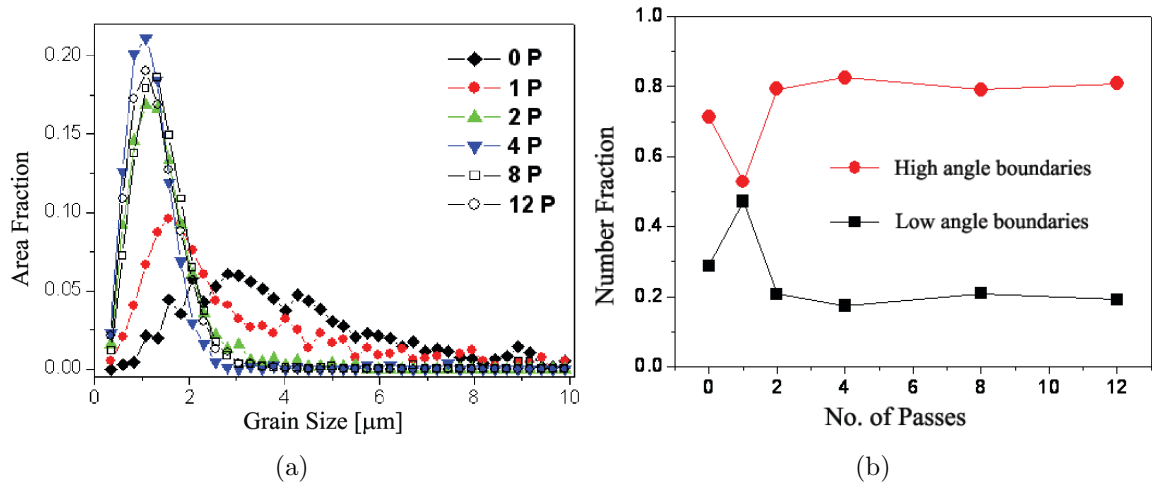


Figure 4.17: (a) Grain size distributions within the range to 10 μm as a function of the number of ECAP passes. (b) Variation of fraction of the HAB and LAB as a function of the number of ECAP passes.

No. of Passes	Area fraction of grains > 10 μm (from EBSD map)
0	17.9 %
1	18.1 %
2	7.9 %
4	2.8 %
8	None
12	None

Table 4.4: Area fraction of large grains as a function of number of ECAP passes

4.5 Microstructural characterization using TEM

The samples for TEM were cut perpendicular to the press direction from the extruded and ECAPed billet, prepared and observed by the procedures mentioned above. The microstructure of extruded samples is shown in Fig.4.18. Fig.4.18 (a) presents the area with small grains of the average size of 2-3 μm . Typical twins are clearly seen in several grains. The (0001) basal texture of individual grains in extruded magnesium alloy observed in EBSD measurements was confirmed by the electron diffraction analysis. The grain boundaries are typically low angle. The area of larger grains is shown in Fig.4.18 (b). This area has a typical heavily deformed structure with high density of tangled dislocations.

Fig. 4.19 presents the microstructure of the specimen after 1 ECAP pass. The bimodal character of the microstructure did not change after the first ECAP pass, the grain size is only slightly smaller in comparison with the extruded material, see Fig. 4.19 (a). However, one significant difference between these two specimens was observed - the character of grain boundaries. One can see many high-angle

grain boundaries with typical thickness fringe band contrast confirming their almost equilibrium state in this micrograph. On the other hand, several grain boundaries remained in a non-equilibrium state with diffuse fuzzy contrast and many dislocations lying in a grain boundary plane were also observed. Several areas with high density of tangled dislocations with no or only exceptional signs of substructure formation were found in this specimen, see Fig. 4.19 (b).

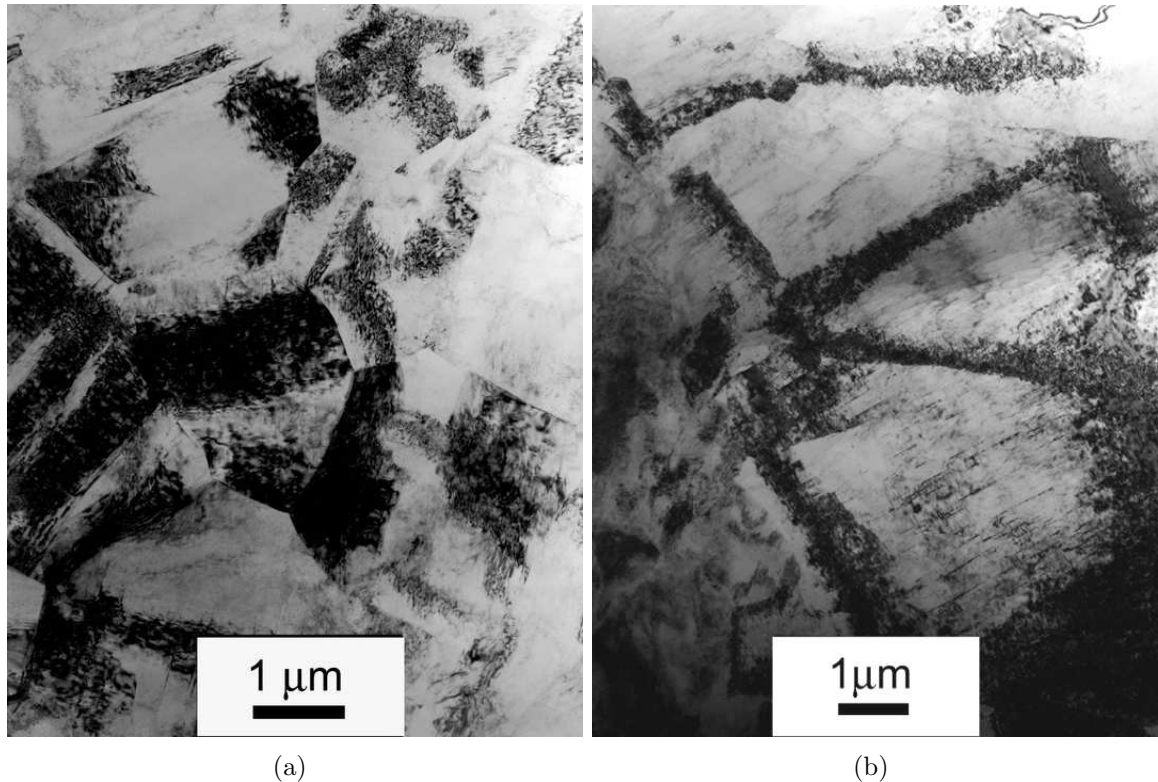


Figure 4.18: Transmission electron micrograph of extruded specimen

Subsequent TEM observation confirmed that the microstructure of extruded and ECAPed samples changed only partly with increasing number of ECAP passes - fine grains were refined only slightly while the large grain zones were refined significantly. Only fine grains of the average grain size in the submicrometer range were observed in the specimen after 8 and 12 ECAP passes. Fig. 4.20 presents the typical microstructure of the sample after 8 passes. One can see that the grains are equiaxed and the average grain size is 800 nm. This ECAPed material has significantly lower density of dislocations and equilibrium grains boundaries. A few newly recrystallized grains of the size of approximately 500 nm and smaller with no dislocations and sharp equilibrium boundaries were also found in the microstructure and one of them is marked in the micrograph with an arrow.

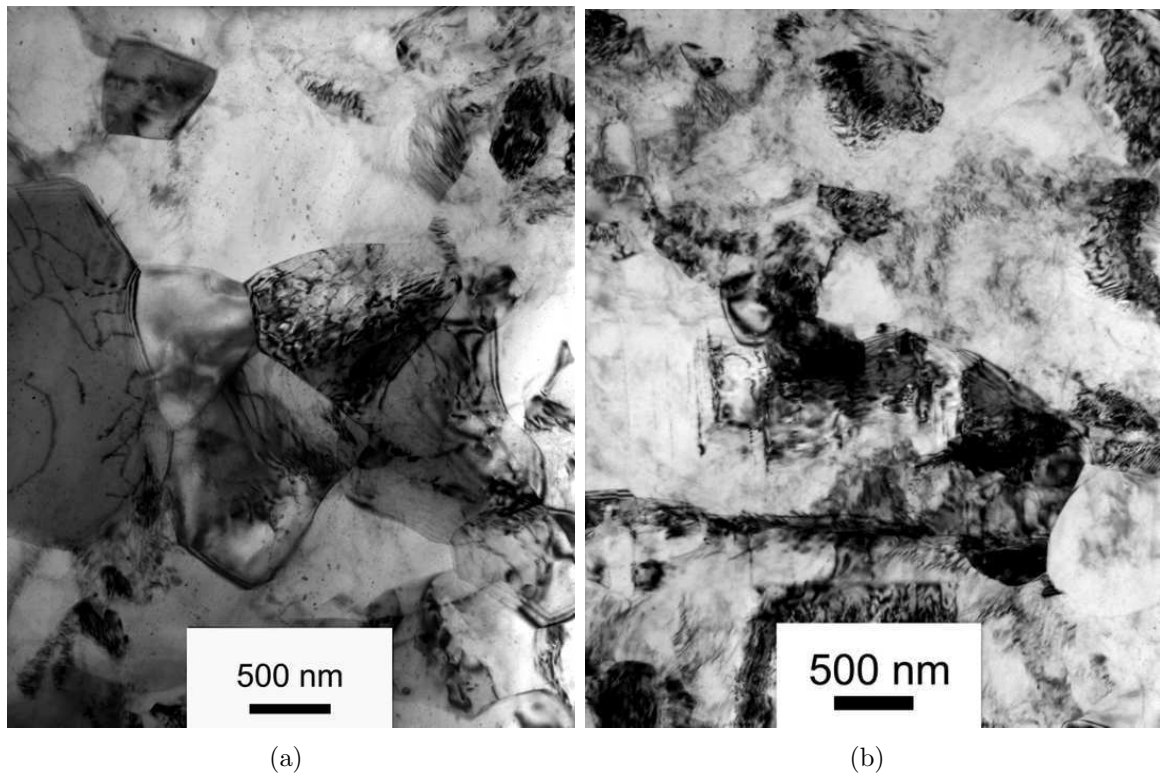


Figure 4.19: Transmission electron micrograph of extruded specimen after 1 ECAP pass

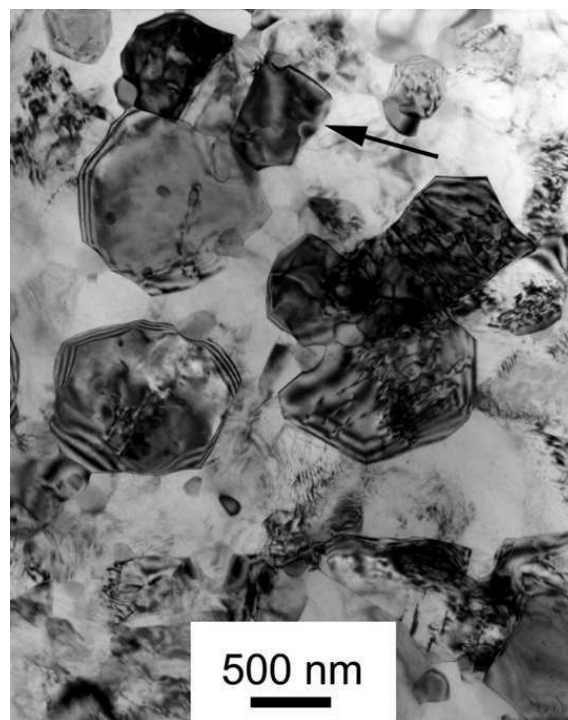


Figure 4.20: Transmission electron micrograph of extruded specimen after 8 ECAP passes

4.6 Corrosion properties

Nyquist diagrams in coordinates with imaginary ($-Z_i$) and real (Z_r) impedance component are the results of electrochemical impedance spectroscopy (EIS) measurements. The values of electrochemical characteristics are determined by the curve shapes, their sizes and the macroscopic character of corrosion process on the sample surface during the measurement. The equivalent circuit shown in Fig. 4.21 is used for the analysis of curves with two capacitive loops. This equivalent circuit is typical for local corroding surfaces, i. e. surfaces with different corrosion products areas (either corrosion waste products or hydride or hydrate oxide passive layers). If the corrosion process (passive layer dissolving and recovery or corrosion waste product formation) is not concentrated only in one part of sample surface, the total polarization resistance equals to the sum of partial polarization resistances R_1 and R_2 . If the curve contains only one capacitive loop, the another equivalent circuit, shown in Fig. 4.22, is used. In this case, only one layer of corrosion products is formed on the sample surface and R_p is the total polarization resistance of the metal-electrolyte interface.

The corrosion properties are investigated at 22 °C and 37 °C. The curve shapes of extruded and ECAPed magnesium alloy AZ31 at 22 °C in Nyquist diagrams indicate the presence of preferential corrosion areas situated on the specimen surface, see Fig. 4.23 - 4.28. The surface is affected by the corrosion unevenly. It was confirmed by the visual control after the exposure test and EIS measurements. The total polarization resistances of the sample surface in 0.1M solution of NaCl after 5 minutes of exposition (designated as 0 h) are approximately equal to the values of 215-250 $\Omega.cm^2$. The samples are designated 0P (only extruded) and 1,...,12P (extruded and subsequently ECAPed). The surface of specimen 12P corrodes with a different mechanism. In this case, a simple curve with only one capacitive loop and total polarization resistance equal to 70 $\Omega.cm^2$ was obtained, see Fig. 4.28. This fact indicates high reactivity of the sample surface but also his low corrosion resistivity, which may be caused by enhanced appearance of cracks, which enlarge the real corrosion surface area.

At the temperature of 22 °C, the total polarization resistance increases with increasing exposition time. The increase is caused by the increase of both components, R_1 and R_2 , up to the exposition time of 72 hours. The passive layer formation of $Mg(OH)_2$ in one part of the sample surface and $MgCl_2$ in the remaining part contributes to the total polarization resistance. The polarization resistance increases significantly after exposition time of 24 and 72 hours because of the increase of pH in the solution. The maximal polarization resistance value 920 $\Omega.cm^2$ was obtained after 72 hours. The total polarization resistance increase is observed in specimens after 1, 2 and 4 ECAP passes as well - the components R_{p1} and R_{p2} increase up to the exposition time 4 hours but the corrosion process changes with additionally increasing exposition times. The polarization resistance of the sample 1P increases up to the value of 370 $\Omega.cm^2$ after 24 hours and remains unchanged after 72 hours. The curve shape indicates the formation of a single dominant corrosion product layer only, probably $MgCl_2$, and the corrosion process is characterized by exfoliation and formation of low-cohesive corrosion products. The polarization resistance depends on the microstructure homogeneity. The homogeneity may cause significant polarization resistance decrease, see Fig. 4.26 after 72 hours. The material loses its corrosion resistivity probably because of the structural elements with different electrochemical stability situated on the sample surface,

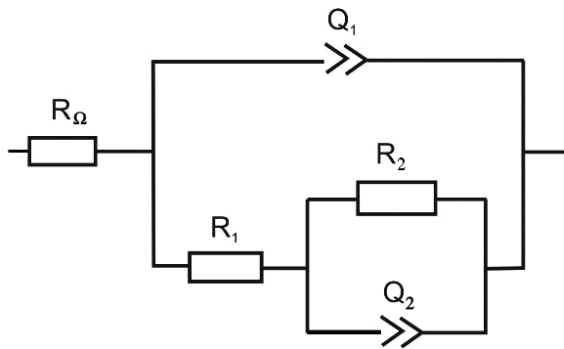


Figure 4.21: The equivalent circuit typical for local corroding surfaces (two capacitive loops in Nyquist diagram)

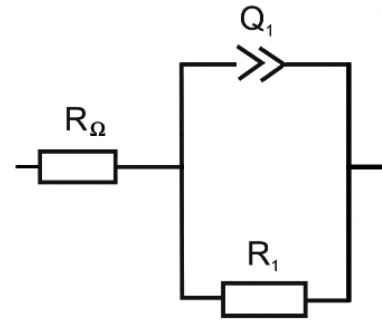


Figure 4.22: The equivalent circuit typical for surfaces with only one corrosion product layer (one capacitive loop in Nyquist diagram)

e.g. impurities or non-recrystallized grains, whose surface is not suitable for corrosion product formation that should protect the metal surface from the corrosion process. The corrosion properties of the sample after 8 ECAP passes (8P) is similar to the extruded sample (0P) - the polarization resistance components increase up to the total value of $750 \Omega.cm^2$ after 24 hours and remains almost unchanged after 72 hours. The 8P sample surface microstructure is homogeneous and does not contain non-recrystallized grains. Therefore, the corrosion product formation is very easy and the specimen surface is protected from the corrosion process.

At the temperature of $37^\circ C$, the polarization resistance changes and the curve shapes are different from the corrosion tests at $22^\circ C$, see Fig. 4.29 - 4.34. The difference is caused by the corrosion kinetics because the corrosion rate depends exponentially on the temperature. The changes in curve shape and therefore the corrosion mechanism are observed in all samples. All measured curves (except that of the sample 1P, see Fig. 4.30) consist of two capacitive loops in the initial stage of corrosion (designated as 0 h). In most cases, only one corrosion product layer with increasing corrosion resistivity is observed with increasing exposition time. The corrosion products may exfoliate because of their weight and make the metal surface exposed. Due to this effect, the electrochemical characteristics degraded in the sample 4P after the exposition time of 40 hours (see Fig. 4.32). The specimen 12P has as poorer corrosion resistance at $37^\circ C$ than at $22^\circ C$. It may be caused by the presence of microcracks in ECAPed billets.

The values of partial polarization resistance of individual specimens at $22^\circ C$ and $37^\circ C$ are summarized in Tab. 4.5 and 4.6, respectively. In the cases represented by the equivalent circuit shown in Fig. 4.21 the both partial polarization resistances R_1 and R_2 are presented in Tab. 4.5 and 4.6. In the case of the simple equivalent circuit shown in Fig. 4.22 a single partial polarization resistance R_1 is presented in mentioned tables.

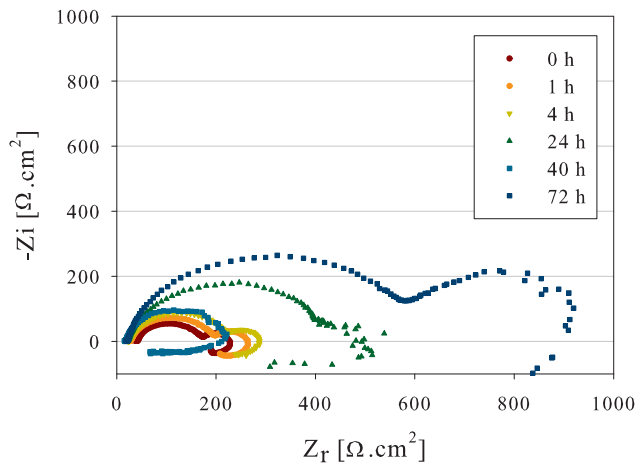


Figure 4.23: The Nyquist diagram of extruded sample (0P) at 22 °C

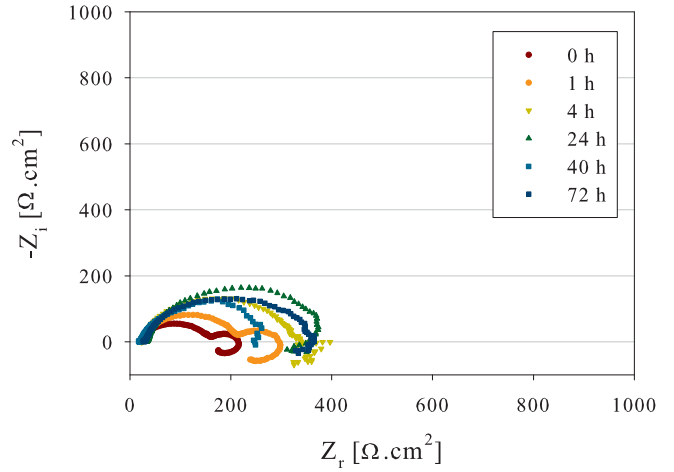


Figure 4.24: The Nyquist diagram of extruded sample after 1 ECAP pass (1P) at 22 °C

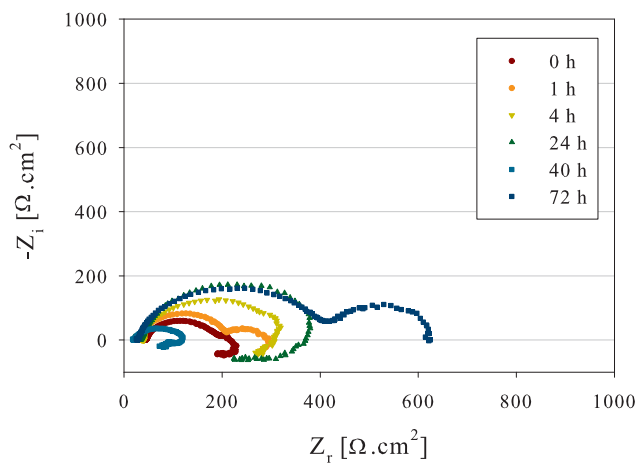


Figure 4.25: The Nyquist diagram of extruded sample after 2 ECAP passes (2P) at 22 °C

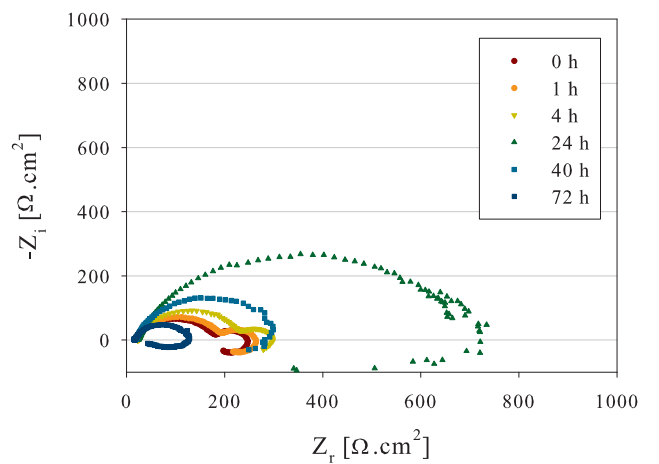


Figure 4.26: The Nyquist diagram of extruded sample after 4 ECAP passes (4P) at 22 °C

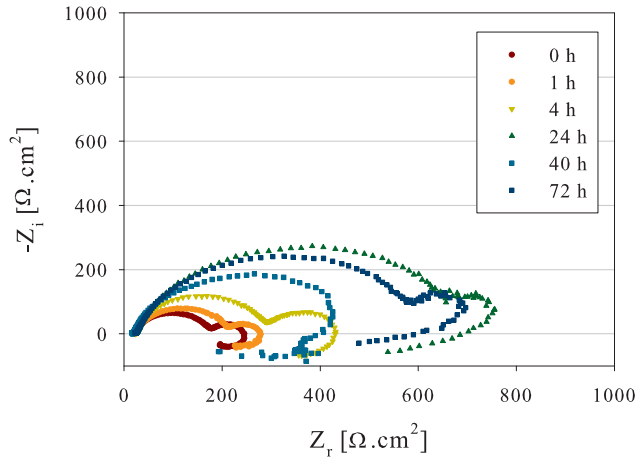


Figure 4.27: The Nyquist diagram of extruded sample after 8 ECAP passes (8P) at 22 °C

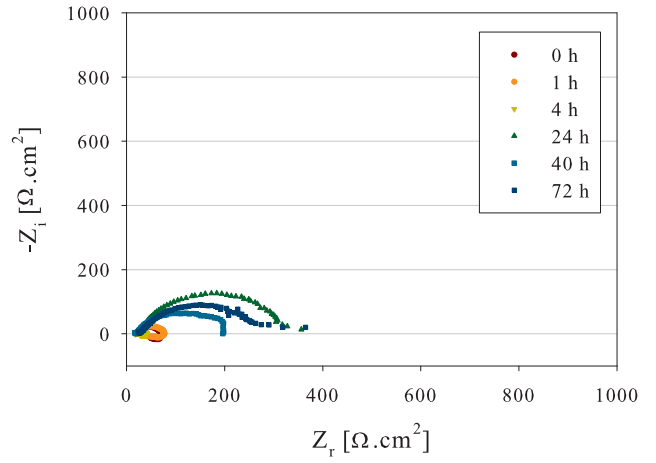


Figure 4.28: The Nyquist diagram of extruded sample after 12 ECAP passes (12P) at 22 °C

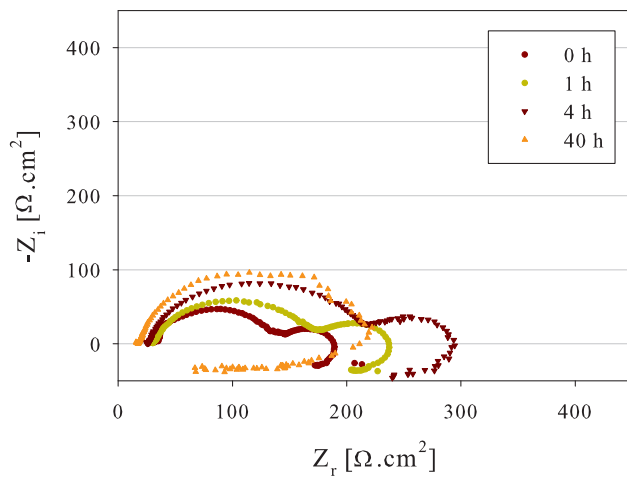


Figure 4.29: The Nyquist diagram of extruded sample (0P) at 37 °C

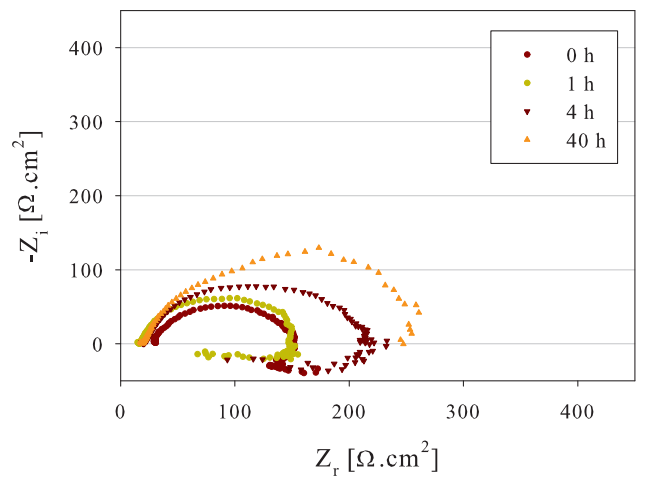


Figure 4.30: The Nyquist diagram of extruded sample after 1 ECAP pass (1P) at 37 °C

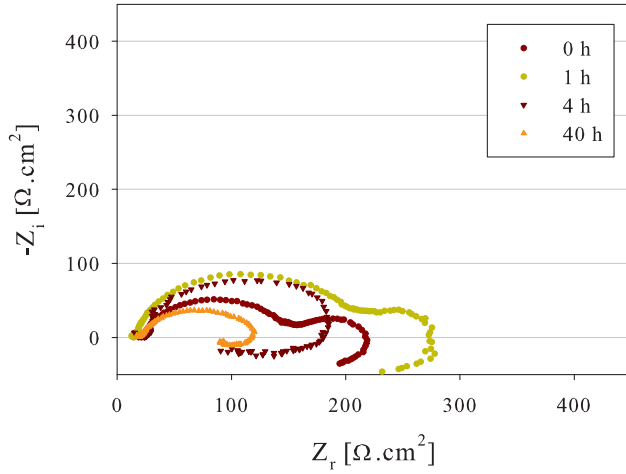


Figure 4.31: The Nyquist diagram of extruded sample after 2 ECAP passes (2P) at 37 °C

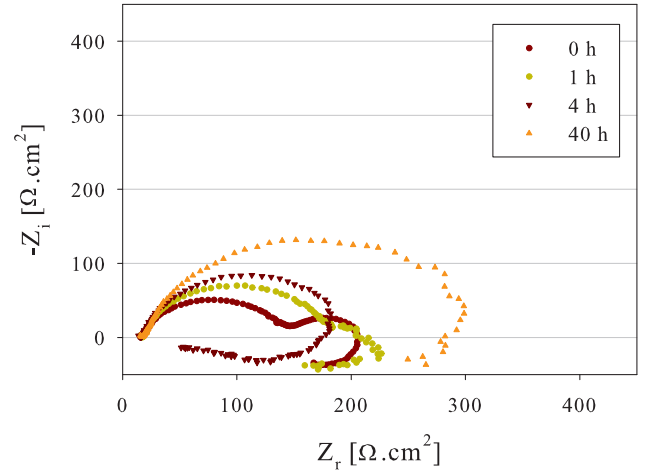


Figure 4.32: The Nyquist diagram of extruded sample after 4 ECAP passes (4P) at 37 °C

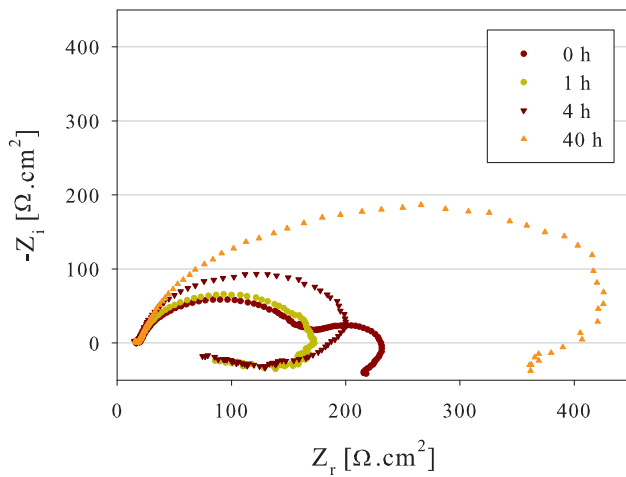


Figure 4.33: The Nyquist diagram of extruded sample after 8 ECAP passes (8P) at 37 °C

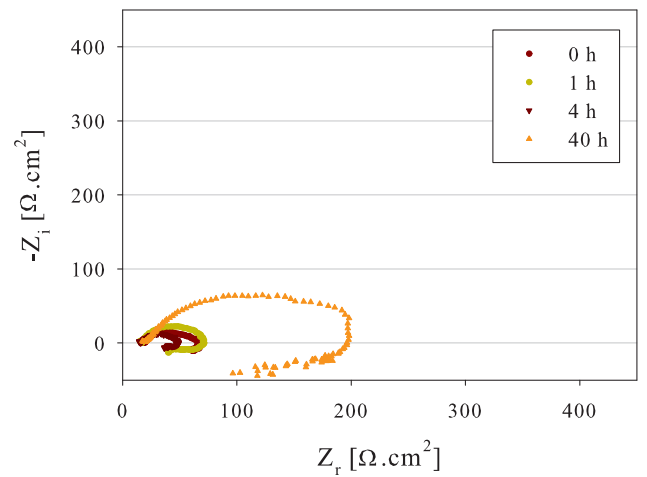


Figure 4.34: The Nyquist diagram of extruded sample after 12 ECAP passes (12P) at 37 °C

Time	0P		1P		2P		4P		8P		12P	
	R_1	R_2										
0 h	131	48	135	63	155	71	155	71	153	68	49	-
1 h	171	61	71	-	187	69	172	66	196	56	56	-
4 h	210	55	267	-	217	-	216	59	272	132	22	-
24 h	434	45	436	43	42	-	683	-	680	-	300	-
72 h	605	343	342	-	388	210	118	-	616	-	267	-

Table 4.5: The partial polarization resistances of extruded and ECAPed specimens at 22 °C

Time	0P		1P		2P		4P		8P		12P	
	R_1	R_2										
0 h	109	63	82	-	125	61	125	62	144	62	38	-
1 h	142	68	146	-	111	-	165	27	157	-	56	56
4 h	194	71	195	-	175	-	189	-	215	-	33	10
40 h	192	18	271	-	102	-	332	-	467	240	200	-

Table 4.6: The partial polarization resistances of extruded and ECAPed specimens at 37 °C

5 Conclusions

In the present work the microstructure evolution, mechanical properties, defect structure and corrosion resistance of ultra-fine grained (UFG) magnesium alloy AZ31 prepared by a combined two-step process (the extrusion and the equal-channel angular pressing (ECAP)) were investigated. The microstructure development was examined by light and transmission electron microscopy and electron backscatter diffraction (EBSD). Mechanical properties were studied by microhardness measurement and tensile tests and the defect structure by positron annihilation spectroscopy (PAS).

The most important results obtained by this investigation can be summarized as follows:

- The microstructure of extruded and ECAPed material became finer during pressing. Light microscopy examination revealed the bimodal structure in specimens up to 4 ECAP passes. The microstructure after 8 ECAP passes became homogeneous.
- The results of tensile tests indicates that the characteristic stress $\sigma_{0.2}$ increases slightly with increasing number of ECAP passes only to the second pass and then decreases significantly with additional ECAP straining. Several models were applied to describe the deformation behaviour of UFG material.
- The results of tensile tests are in accordance with the results of PAS. The dislocation density was found to increase up to the second pass and to decline continuously up to the twelfth pass.
- EBSD measurements confirmed that the microstructure of extruded and ECAPed material has a bimodal distribution of grain sizes. The bimodal distribution becomes homogeneous with increasing number of ECAP passes and no remaining large grains were observed after 8 passes. The average grain size after 12 passes of ECAP straining is in submicrometer range and the fraction of high-angle grain boundary (HAGB) is approximately equal to 80%.
- The observation in transmission electron microscope proved the EBSD measurements.
- Corrosion tests demonstrated that the corrosion properties depend on the number of ECAP passes. Corrosion resistivity is related to many microstructure aspects, in particular the microstructure homogeneity or the presence of non-recrystallized grains. The corrosion mechanism depends on exposure time. The corrosion products may form one or two layers with rather complicated structure (uneven corrosion areas, pores etc.). The extruded specimens after 8 ECAP passes show the best corrosion resistance mainly due to their homogenous microstructure and relatively low density of microcracks in the ECAPed material.

6 Prospective continuation of the research

The results of this investigation indicated many unique properties of ultra-fine grained AZ31 alloy processed by ECAP. However, further work is necessary to obtain a more detail description and deeper understanding of various physical properties of the material.

Some interesting topics which might be worth of further investigation include:

- the processing of extruded AZ31 polycrystals by unconventional ECAP routes [100] which is currently a promising way allowing to obtain new microstructure features in magnesium alloy,
- processing of the material by another SPD technique, in particular the technique of high pressure torsion seems to be a promising alternative and probably more effective way of grain refinement which attracts growing attention of research in SPD community,
- using non-conventional techniques of material processing, as e.g. rotary swaging which proved to result in microstructures and physical properties which are superior to those of material processed by classical SPD techniques, in particular in other commercial magnesium alloys [101, 102, 103].

7 Bibliography

- [1] K. Kubota, M. Mabuchi, K. Higashi: *Journal of Materials Science* 34(10) (1999) 2255.
- [2] R. von Mises: *Z. Angew. Math. Mech.*, 8 (1928) 161.
- [3] A. Galiyev, R. Kaibyshev, G. Gottstein: *Acta Mater.* 49 (2001) 1199.
- [4] X. S. Huang, K. Suzuki, A. Watazu, I. Shigematsu, N. Saito: *Effects of Homogenization Treatment on Mechanical Properties of Hot-Rolled AZ31 Magnesium Alloy*, vol. 561, Transtec Publications (2007) p. 255.
- [5] M. C. Zhao, M. Liu, G. L. Song, A. Atrens: *Advanced Engineering Materials* 10 (1-2) (2008) 93.
- [6] E. A. Ball, P. B. Prangnell: *Scripta Metallurgica et Materialia* 31 (1994) 111.
- [7] J. Becker, B. Fischer, K. Schemme: *Light weight construction using extruded and forged semi-finished products made of magnesium alloys. Magnesium Alloys and their Applications* (1998) p. 15-28.
- [8] A. Akhtar, E. Teghtsoonian: *Philosophical Magazine* 25 (1972) 897.
- [9] J. Balik, M. Janecek, P. Lukac: *Mater Sci Eng A* 159 (1992) 143.
- [10] H. E. Friedrich, B. L. Mordike: *Magnesium technology: metallurgy, design data, applications* (2006).
- [11] A. Serra, D. J. Bacon, R. C. Pond: *Metallurgical and Materials Transactions A* 33 (2002) 809.
- [12] R. Z. Valiev, Y. Estrin, Z. Horita, T. G. Langdon, M. J. Zehetbauer, Y. T. Zhu: *JOM* 58 (4) (2006) 33.
- [13] E. O. Hall: *Proc. Roy. Soc. B* 64 (1951), 747.
- [14] N. J. Petch: *J. Iron Steel Inst.* 174 (1953) 25.
- [15] Y. T. Zhu, T. C. Lowe, T. G. Langdon: *Scripta Mater.* 51 (2004) 825.
- [16] U. Erb, A. M. El-Sherik, G. Palumbo, K. T. Aust: *Nanostruct. Mater.* 2 (1993) 383.
- [17] R. Birringer, H. Gleiter, H. P. Klein: *Phys. Lett. A* 102 (1984) 365.
- [18] J. S. Benjamin: *Metall. Trans.* 1 (1970) 2943.
- [19] D. B. Witkin, E. J. Lavernia: *Prog. Mater. Sci.* 51 (2006) 1.
- [20] J. T. Wang: *Mater. Sci. Forum* 503-504 (2006) 363.
- [21] C. Srinivasan: *Curr. Sci.* 92 (2007) 279.

- [22] O. D. Sherby , J. J. Wadsworth: Mater. Proc. Tech. 117 (2001) 347.
- [23] P. W. Bridgman: Studies in large plastic flow and fracture. New York (NY): McGraw - Hill (1952).
- [24] V. M. Segal, V. I. Reznikov, A. E. Drobyshevskiy, V. I. Kopylov: Plastic working of metals by simple shears, Russian Metall (1981) 1:99-105.
- [25] R. I. Kuznetsov, V. I. Bykov, V. P. Chernyshev, V. P. Pilyugin, N. A. Yefremov, A. V. Pasheyev: Plastic deformation of solid bodies under pressure - 1: Equipment and methods. Preprint 4/85, IFM UNTs AN SSSR, Sverdovsk, USSR (1985).
- [26] N. A. Smirnova, V. I. Levit, V. I. Pilyugin, R. I. Kuznetsov, L. S. Davydova, V. A. Sazonova: Fiz. Metal. Metalloved 61 (6) (1986) 1170.
- [27] Y. Saito, H. Utsunomiya, N. Tsuji, T. Sakai: Acta Mater. 47 (1999) 579.
- [28] W. M. Thomas, E. D. Nicholas, J. C. Needham, M. G. Murch, P. Temple-Smith, C. J. Dawes: GB Patent No. 9125978.8 (1991), US Patent No. 5460317 (1995).
- [29] R. S. Mishra, M. W. Mahoney, S. X. McFadden, N. A. Mara, A. K. Mukherjee: Scripta Mater. 42 (2000) 163.
- [30] Y. T. Zhu, H. Jiang, J. Huang, T. C. Lowe: Metall. Mater. Trans A 32 (2001) 1559.
- [31] Y. T. Zhu, T. C. Lowe, H. Jiang, J. Huang: US Patent No. 6197129 (2001).
- [32] G. A. Salishche, O. R. Valiahmety, R. M. Galeev: J Mater Sci 28 (1993) 2898.
- [33] O. Sitdikov, T. Sakai, A. Goloborodko, H. Miura, R. Kaibyshev: Mater Trans 45 (2004) 2232.
- [34] Y. Beygelzimer, V. Varyukhin, D. Orlov, S. Synkov, A. Spuskanyuk, Y. Pashinska. In: M. J. Zehetbauer, R. Z. Valiev, editors. Nanomaterials by severe plastic deformation. Weinheim, Germany: Wiley-VCH Verlag (2004) p. 511.
- [35] V. N. Varyutkhin, Y. Beygelzimer, S. Synkov, D. Orlov: Mater Sci Forum 503-504 (2006) 335.
- [36] J. Richert, M. Richert: Aluminium 62 (1986) 604.
- [37] M. Richert, Q. Liu, N. Hansen: Mater Sci Eng A260 (1999) 275.
- [38] V. M. Segal: USSR Patent No. 575892 (1977).
- [39] H. K. Lin, J. C. Huang, T. G. Langdon: Mater. Sci. Eng. A 402 (2005) 250.
- [40] C. Xu, M. Furukawa, Z. Horita, T. G. Langdon: Mater. Sci. Eng. A 398 (2005) 66.
- [41] E. Rabkin, I. Gutman, M. Kazakevich, E. Buchman, D. Gorni: Mater. Sci. Eng. A 396 (2005) 11.

- [42] N. Krasilnikov, W. Lojkowski, Z. Pakiela, R. Valiev: *Mater. Sci. Eng. A* 397 (2005) 330.
- [43] V. V. Latysh, I. P. Semenova, G. H. Salimgareeva, I. V. Kandarov, Y. T. Zhu, T. C. Lowe, R. Z. Valiev: *Mater. Sci. Forum* 503-504 (2006) 763.
- [44] H. S. Kim, W. S. Ryu, M. Janecek, S. C. Baik, Y. Estrin: *Adv. Eng. Mater.* 7 (2005) 43.
- [45] Y. Li, T. G. Langdon: *J. Mater. Sci.* 35 (2000) 1201.
- [46] G. J. Raab, R. Z. Valiev, T. C. Lowe, Y. T. Zhu: *Mater. Sci. Eng. A* 382 (2004) 30.
- [47] P. B. Berbon, M. Furukawa, Z. Horita, M. Nemoto, T. G. Langdon: *Metall Mater Trans* 30A (1999) 1989.
- [48] Y. Iwahashi, J. Wang, Z. Horita, M. Nemoto, T. G. Langdon: *Scripta Mater.* 35 (1996) 143.
- [49] K. Furuno, H. Akamatsu, K. Oh-ishi, M. Furukawa, Z. Horita, T. G. Langdon: *Acta Mater.* 52 (2004) 2497.
- [50] Z. Horita, M. Furukawa, M. Nemoto, T. G. Langdon: *Mater Sci Tech* 16 (2000) 1239.
- [51] V. M. Segal: *Mater. Sci. Eng. A* 197 (1995) 157.
- [52] K. Nakashima, Z. Horita, M. Nemoto, T. G. Langdon: *Mater. Sci. Eng. A* 281 (2000) 82.
- [53] M. Nemoto, Z. Horita, M. Furukawa, T. G. Langdon: *Metals Mater* 4 (1998) 1181.
- [54] S. Lee, T. G. Langdon: *Mater Res Soc Symp Proc* 601 (2000) 359.
- [55] K. Nakashima, Z. Horita, M. Nemoto, T. G. Langdon: *Acta Mater* 46 (1998) 1589.
- [56] A. Yamashita, D. Yamaguchi, Z. Horita, T. G. Langdon: *Mater Sci Eng A* 287 (2000) 100.
- [57] D. H. Shin, J. J. Pak, Y. K. Kim, K. T. Park, Y. S. Kim: *Mater Sci Eng A* 325 (2002) 31.
- [58] R. Z. Valiev, I. V. Alexandrov, T. C. Lowe, Y. T. Zhu: *J Mater Res* 17 (2002) 5.
- [59] Ch. Xu, K. Xia, T. G. Langdon: *Mater Sci Eng A* 527 (2009) 205.
- [60] Ch. Xu, K. Xia, T. G. Langdon: *Acta Mater* 55 (2007) 2351.
- [61] Ch. Xu, S. Schroeder, P. B. Berbon, T. G. Langdon: *Acta Mater* 58 (2010) 1379.
- [62] M. V. Degtyarev, T. I. Chashchukhina, L. M. Voronova, A. M. Patselov, V. P. Pilyugin: *Acta Mater.* 55 (2007) 6039.

- [63] R. Z. Valiev, R. K. Islamgaliev, I. V. Alexandrov: Prog Mater Sci 45 (2000) 103.
- [64] A. P. Zhilyaev, S. Lee, G. V. Nurislamova, R. Z. Valiev, T.G. Langdon: Scripta Mater 44 (2001) 2753.
- [65] A. P. Zhilyaev, G. V. Nurislamova, B. K. Kim, M. D. Baro, J. A. Szpunar, T. G. Langdon: Acta Mater. 51 (2003) 753.
- [66] Z. Horita, D. J. Smith, M. Furukawa, M. Nemoto, R. Z. Valiev, T. G. Langdon: J Mater Res 11 (1996) 1880.
- [67] Y. Iwahashi, Z. Horita, M. Nemoto, T. G. Langdon: Metall Mater Trans 29A (1998) 2503.
- [68] A.P. Zhilyaev, K. Oh-ishi, T.G. Langdon, T.R. McNelley: Mater Sci Eng A 410-411 (2005) 277.
- [69] Y. Harai, Y. Ito, Z. Horita: Scripta Mater. 58 (2008) 469.
- [70] N. Tsuji, Y. Saito, S. H. Lee, Y. Minamino: Adv. Eng. Mater. 5 (2003) 338.
- [71] G. Krallics, J. G. Lenard: Journ. Mater. Proc. Tech. 152 (2004) 154.
- [72] R. Z. Valiev, R. K. Islamgaliev, I. V. Alexandrov: Prog. Mater. Sci., 45 (2000) 103.
- [73] J. Huang, Y. T. Zhu, H. Jiang, T. C. Lowe: Acta Mater. 49 (2001) 1497.
- [74] R. Lapovok et al.: J. Mater. Sci. 40 (2005) 1.
- [75] Y. Estrin, L. A. Tóth, Y. Bréchet and H. S. Kim Mater. Sci. Forum 503-504 (2006) 675.
- [76] M. Zehetbauer, T. Ungár, R. Král, A. Borbély, E. Schafner, B. Ortner, H. Amenitsch, S. Bernstorff: Acta. Mater. 47 (1999) 1053.
- [77] R. Z. Valiev: Nature Mater. vol. 3 (2004) 511.
- [78] Z. Horita, K. Ohashi, T. Fujita, K. Kaneko, T. G. Langdon: Adv. Mater. 17 (2005) 1599.
- [79] N. Q. Chinh, P. Szommer, Z. Horita and T. G. Langdon: Adv. Mater. 18 (2006) 34.
- [80] H. W. Höppel, M. Kautz, C. Xu, M. Murashkin, T. G. Langdon, R. Z. Valiev, H. Mughrabi: Int. Journal of Fatigue 28, 9 (2006) 1001.
- [81] C. Xu, M. Furukawa, Z. Horita, T. G. Langdon: J. Mater. Perform. 13 (2004) 683.
- [82] A. V. Kulkarni, I. Karaman, Z. P. Luo, Y. I. Chumlyakov: Ultrafine Grained Materials III, Warrendale, PA : TMS (2004) 481.
- [83] V. Skripnyuk, E. Rabkin, Y. Estrin, R. Lapovok: Acta Mater. 52 (2004), 405.
- [84] ASM internacional: Binary Alloy Phase Diagrams (1990).

- [85] G. E. Dieter: Mechanical Metallurgy, Mc. Graw Hill (1986).
- [86] Z. Kvíčalová: Mechanické vlastnosti a vývoj mikrostruktury jemnozrnných polykrystalů vybraných hořčíkových slitin, bachelor thesis, Praha, MFF UK (2008) p.11.
- [87] D. B. Williams, C. B. Carter: Transmission Electron Microscopy, Plenum Press, NY and London (1996).
- [88] N. Q. Chinh, G. Horváth, Z. Horita, T. G. Langdon: Acta Mater 52 (2004) 3555.
- [89] U. F. Kock: J. Eng. Mater. Tech 98 (1976) 76.
- [90] Y. Estrin, H. Mecking: Acta Metall. 32 (1984) 57.
- [91] G. A. Malygin: Phys. Stat. Sol. (a) 119 (1990) 423.
- [92] F. Bečvář, J. Čížek, L. Lešták, I. Novotný, I. Procházka, F. Šebesta: Nucl. Instr. Meth. A 557 (2000) 443.
- [93] I. Procházka, I. Novotný, F. Bečvář: Mater. Sci. Forum 772 (1997) 255.
- [94] J. Čížek, I. Procházka, B. Smola, I. Stulíková, R. Kužel, Z. Matěj, V. Cherkaska: Phys. Stat. Sol. (a) 466 (2006) 203.
- [95] P. Hautojärvi, C. Corbel: A. Dupasquier, A. P. Mills (Eds.), Proceedings of the International School of Physics "Enrico Fermi", Course CXXV, IOS Press, Varena (1995) 491-562.
- [96] M. Abdelrahman, E. Badawi, Jpn. J. Appl. Phys. 35 (1996) 4728.
- [97] J. Bohlen, S. Yi, J. Swiostek, D. Letzig, H. G. Brokmeier, K. U. Kainer: Scripta Mater. 53 (2005) 259.
- [98] Y. Estrin, S. Yi, H. G. Brokmeier, Z. Zuberova, S. C. Yoon, H. S. Kim, R. J. Hellmig: Inter. J. Mater. Res. 99 (2008) 50.
- [99] S. E. Ion, F. J. Humphreys, S. H. White: Acta Mater. 30 (1982) 1909.
- [100] S. N. Mathaudhu, L. J. Kecskes, J. Im, D. C. Foley, M. Al-Maharbi, I. Karaman, K. T. Hartwig: Superior Grain Refinement via Intelligent ECAE Processing of Materials, Ultrafine Grained Materials Sixth International Symposium, 2010 TMS Annual Meeting.
- [101] J. Müller, M. Janeček, L. Wagner: Mater. Sci. Forum 584-586 (2008). 858.
- [102] M. Shahzad, M. Janeček, L. Wagner: Int. Jour. Mat. Res. 100 (2009) 370.
- [103] M. Shahzad, L. Wagner: Scripta Mat. 60 (2009) 536.